Neuron

Article

Distinct brain regions map olfactory and visual spaces

Graphical abstract

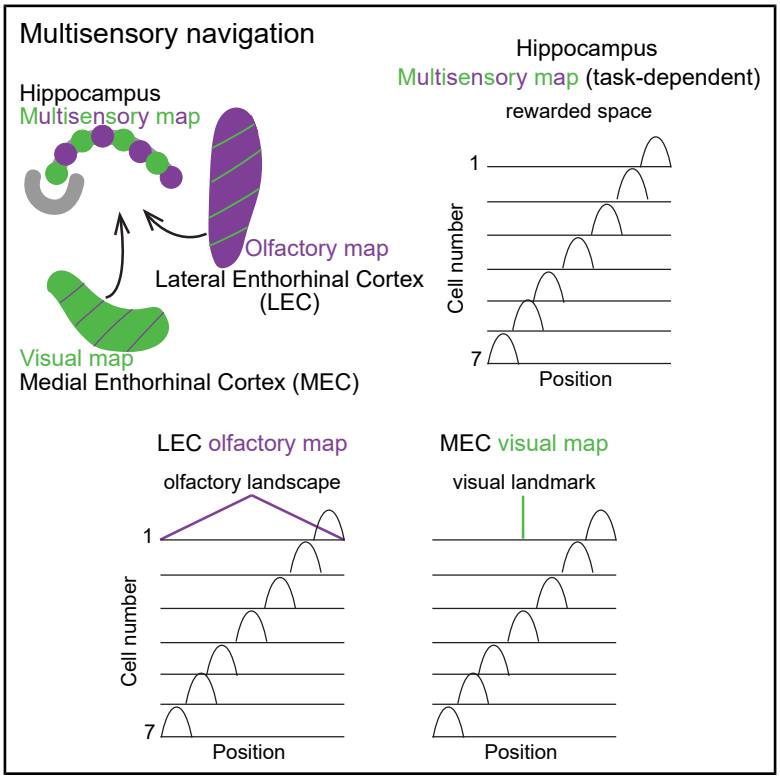

Highlights

- Multisensory virtual reality used to dissect components of the cognitive map
- LEC maps olfactory space during navigation, regardless of its behavioral relevance
- MEC maps visual space during navigation, regardless of its behavioral relevance
- CA1 flexibly maps the behaviorally relevant sensory space during navigation

Authors

Heydar Davoudi, Jason R. Climer, John B. Issa, Daniel A. Dombeck

Correspondence

d-dombeck@northwestern.edu

In brief

The neural circuitry underlying multisensory integration for navigation and spatial memory is poorly understood. Here, Davoudi et al. discover modality-specific maps in different divisions of the entorhinal cortex, which the hippocampus then appears to combine in a flexible manner that depends on task demands.

Davoudi et al., 2026, Neuron *114*, 2868–2883
August 5, 2026
https://doi.org/10.1016/j.neuron.2026.03.008

CellPress

CellPress

Neuron

Article

Distinct brain regions map olfactory and visual spaces

Heydar Davoudi,[1] Jason R. Climer,[1,2] John B. Issa,[1] and Daniel A. Dombeck[1,3,*]
[1]Department of Neurobiology, Northwestern University, Evanston, IL, USA
[2]Department of Molecular and Integrative Physiology, University of Illinois, Champaign, IL, USA
[3]Lead contact
*Correspondence: d-dombeck@northwestern.edu
https://doi.org/10.1016/j.neuron.2026.03.008

SUMMARY

The hippocampus contains a multisensory cognitive map that incorporates spatial cues from across the senses, such as vision and olfaction. However, how primary sensory information transforms along pathways to the hippocampus into this single, combined map is largely unknown. Specifically, does the hippocampus generate or inherit the multisensory map of space? Here, we used multisensory virtual reality and large-scale functional imaging to determine whether and how the main input regions to hippocampus, the lateral and medial entorhinal cortices (LECs and MECs, respectively), map olfactory, and visual sensory spaces in navigating mice. We discovered that, unlike multisensory mapping in the hippocampus, LEC preferentially maps olfactory space, whereas MEC preferentially maps visual space, regardless of the behavioral relevance of the spaces. This establishes the existence of largely independent brain maps for different sensory spaces, suggesting that the hippocampus builds the cognitive map by combining modality-specific maps from pre-synaptic cortical regions.

INTRODUCTION

Navigation often requires animals to integrate cues from multiple sensory modalities into a cohesive and unified internal representation of space (Figure 1A)—a cognitive map.[1–9] The hippocampus plays the central role in this process,[4,10–14] as its place cells map multisensory spaces in a task-dependent manner.[10,15–18] Yet, the mapping of different sensory modality spaces (versus primary sensory encoding; Figure 1B) during navigation has not been systematically explored, even a single synapse upstream from the hippocampus, in the entorhinal cortex. Therefore, it is not yet known whether the hippocampus generates or inherits the multisensory map of space.

The entorhinal cortex is anatomically divided into lateral (LEC) and medial (MEC) subdivisions, which differ in their anatomical inputs and presumed functional roles.[19–21] LEC receives a large fraction of its input from parahippocampal and olfactory areas.[19,21] During navigation, it has been shown to encode visual objects[22,23] and rewards in visual virtual environments[24–26] and to be involved in odor-associative learning in navigation[27] and non-navigation-based tasks.[28–30] Importantly, while these prior studies suggest that LEC might be able to form olfactory-visual multisensory spatial maps, none establish that LEC actually contains such a map of space during navigation. However, if it does form spatial maps, they may also be olfactory-specific, since previously described representations of other sensory modalities, such as vision, might instead relate to context or behavioral states.[23,24,31–35] Thus, currently, evidence that LEC can map olfactory and/or visual spaces is lacking.

MEC, on the other hand, contains the well-known spatially tuned grid cells,[36–38] and other spatial cells,[37,39,40] in rodents during navigation of multisensory environments. The firing fields of grid cells were shown, in some conditions, to persist in the dark,[36] which could mean that grid cells map multisensory spaces, since they might be driven by sensory modalities other than vision. Indeed, while MEC does receive input from olfactory areas,[19] it also receives a larger fraction of input from visual areas,[21] and other studies under dark conditions found largely degraded grid cell firing.[41–44] So it is also possible that MEC preferentially maps spaces defined by visual cues.[38,45–49] Thus, it remains an open question whether MEC can map both olfactory and visual spaces and participate in olfactory-visual multisensory spatial processing.

Overall, it remains unknown whether and how the presynaptic regions of the hippocampus map different senses during multisensory navigation. Here, we employed a multisensory virtual reality (VR) system enabling precise and independent control of olfactory and visual spatial cues, combined with large-scale two-photon (2-P) functional imaging in hippocampal CA1, LEC, and MEC of mice performing different navigation tasks (Figure 1C). We found that LEC preferentially maps olfactory space and MEC preferentially maps visual space, both with significantly less task-specific modulation compared with CA1. These results uncover parallel modality-specific pathways

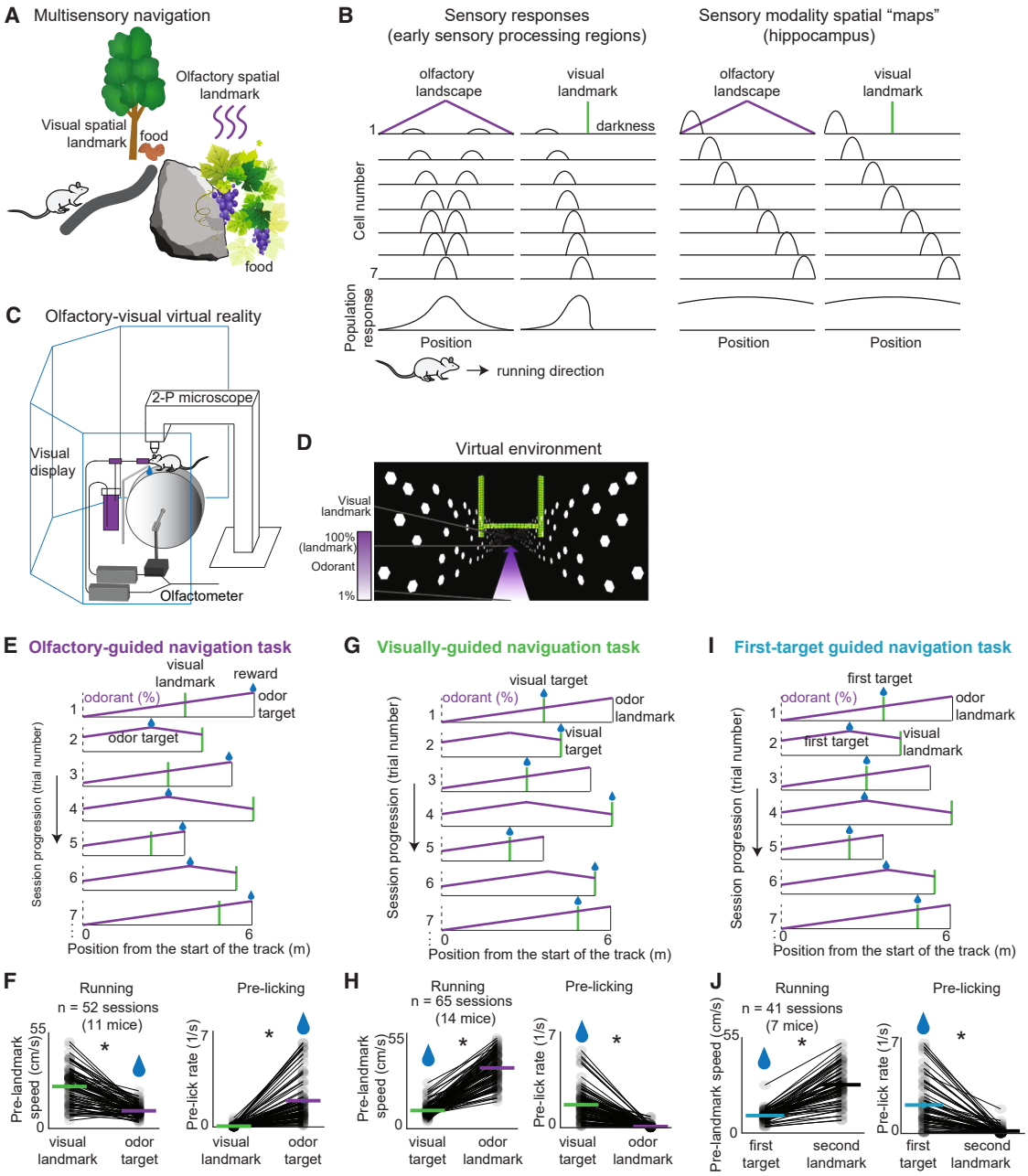

Figure 1. Mice perform diverse multisensory virtual navigation tasks

(A) Mouse in a multisensory habitat using visual and olfactory landmark-based navigation. Animals may rely on visual landmarks, olfactory gradients, or a combination of both to find food.

(B) Schematic examples of how early sensory processing areas (left, e.g., olfactory bulb, retina/LGN) and cognitive regions (right) are likely to encode an environment defined by either a center-peaked olfactory gradient (purple) or a single visual landmark (green) in a mouse running through the environment. In early sensory processing regions, encoding is expected to be driven directly by the properties of the sensory cues at each location. Cognitive brain regions, on the other hand, are expected to form a continuous map of these environments, in which every location is uniquely encoded, even different locations with the same sensory cues (as in the olfactory-defined environment) or with no sensory cues (as in the last half of the visually defined environment).

(C) The visual-olfactory multisensory experimental setup, including a head-fixed mouse running on a cylindrical treadmill surrounded by a VR display, an olfactory VR system ending with a nosecone over the mouse's nose, and a water reward delivery system; all under a 2P microscope.

(D) In each traversal lap, the mouse experiences a visual landmark (green archway), visual optic flow on the walls, and an odor landmark defined as the peak of an odorant gradient (purple, not visible to mice).

(E) The olfactory-guided navigation task. In each lap, mice experience a different odor target location (purple), visual landmark location (green bar), and track length, and only receive a water reward (blue droplet) at the odor target, in which the odorant concentration gradient peaks.

(legend continued on next page)

containing relatively independent spatial maps, which could be used to construct a unified, task-specific multisensory cognitive map in the hippocampus. Thus, while the hippocampus constructs a flexible, goal-directed spatial map for action planning,[18] less flexible elemental spatial maps of individual sensory modalities exist presynaptically within distinct subdivisions of the entorhinal cortex.

RESULTS

Mice navigated a multisensory virtual linear track that simultaneously provided two independent yet superimposed olfactory and visual spaces.[17,50,51] Inspired by the mouse's innate ability to employ a gradient ascent algorithm to reach an odor source,[52–55] we designed an olfactory space based on a pine-scented linear odor gradient of constant slope, in which the "odor landmark" was defined by the track location of the peak odorant concentration (Figure 1D). The visual space was defined entirely by a large green archway (the "visual landmark") within two infinite white-dot walls that provided optic flow. To determine whether CA1, LEC, and MEC map different sensory spaces and how the task-relevance of the sensory modality impacts spatial mapping, we used three navigation tasks (olfactory-guided, visually-guided, and first-target-guided) with identical olfactory-visual sensory experience but different rewarding strategies. Depending on the respective task, the water-rewarded target was defined either as the olfactory landmark, visual landmark, or whichever landmark appeared first.

To establish the neural representation of visual, olfactory, and multisensory spaces during different tasks, we recorded from neuronal populations in CA1, LEC, and MEC using 2-P calcium imaging (Figure 2A; 45,277 cells, 15 mice, 153 sessions; different planes were imaged across sessions). CA1 imaging was performed through hippocampal windows,[56] whereas LEC and MEC were accessed via implanted microprisms.[24,57] This experimental framework enabled us to determine whether and how the entorhinal-hippocampal network maps different sensory modality spaces during multisensory navigation.

LEC maps olfactory space

While substantial evidence demonstrates the multisensory nature of hippocampal maps,[12,14,17,18,58] it remains unclear whether multisensory maps exist one synapse upstream. To determine whether LEC and MEC map olfactory, visual, or both sensory modality spaces, we first used the "olfactory-guided" navigation task, in which head-fixed mice received water rewards only at the odor target location of the multisensory linear track (Figure 1E). Therefore, the olfactory space was behaviorally relevant, and the visual space was not, serving as a distractor. On each trial, mice traversed the track and received a reward at the odor target regardless of whether it appeared first or second. At the second landmark, they experienced a brief pause (1-s freeze followed by 2-s without cues) before the start of the next trial. To ensure that mice relied on sensory cues rather than idiothetic path integration (e.g., step counting[59]), the order and positions of olfactory and visual landmarks and total track length were pseudo-randomized on each trial (Figure 1E). Track lengths ranged from 3.55 to 6.00 m (mean ± SD: 5.26 ± 0.6 m), landmark spacing from 1.15 to 3 m (2.01 ± 0.5 m), and the visual landmark appeared at one of seven possible positions (STAR Methods). Mice (n = 11; 52 sessions) showed strong task engagement, exhibiting anticipatory slowing and licking before the odor target (Figures 1F, S1A, and S1B).

Next, we imaged neural populations within the hippocampal-entorhinal network. The task design allowed us to dissociate the neural mapping of visual and olfactory spaces based on each mouse's position relative to the corresponding sensory landmarks. In addition to these sensory-defined spaces, the design also enabled analysis of neural mapping relative to the track start, as well as abstract spatial mapping of the first landmark (i.e., the first cue encountered, regardless of modality; examined in detail below). We first imaged CA1; for each active CA1 neuron, we calculated the mean significant calcium transients ($\Delta F/F_0$) and the spatial information of its spatial tuning with respect to four different coordinates (i.e., track start, visual landmark, odor landmark, and modality-invariant first landmark; STAR Methods; Figures 2B, S1C, S1E, and S2A). Out of 5,164 active CA1 cells, 2,328 had significant spatial information in at least one coordinate (3 mice, 15 sessions, 5,164 active cells; 344.3 ± 20.1 (mean ± SEM) active cells per session; 46.5% ± 3.3% spatial cells), and we defined each neuron's preferred space as the one with the highest significant spatial information. This process identified four spatial cell types (i.e., start spatial, visual spatial, odor spatial, and first-landmark spatial cells), and we visualized the spatial tuning of these four populations in peak-sorted, cross-validated heatmaps (Figures 3A and 3B). This analysis revealed significantly more odor spatial cells than other cell types; however, a significant fraction of start and visual spatial cells remained, and very few first-target spatial cells (Figure 3B). The heat maps (Figure 3A), along with peak distribution histograms of the different CA1 spatial cell populations (Figures 3G and S1D), revealed mapping of the different spaces.

(F) Task engagement for all sessions quantified by anticipatory slowing (left) and lick increase (right) relative to odor target (purple) but not visual landmark (green). 11 mice; n = 52 sessions; two-tailed Wilcoxon signed-rank test: speed, z(51) = 6.1, p = 1.0e−9; licking, z = –6.3, p = 3.7e−10. *p < 0.05.

(G) The visually-guided navigation task. In each lap, mice experience a different odor landmark location, visual target location, and track length, and only receive a water reward at the visual target.

(H) Task engagement is quantified by anticipatory behaviors such as pre-reward slowing and increased licking prior to reaching the visual target, but not in response to the olfactory landmark for all sessions. 14 mice, n = 65 sessions; two-tailed paired Wilcoxon signed-rank test: speed, z(64) = –7.0, p = 2.4e−12; licking, z = 7.0, p = 2.4e−12. *p < 0.05.

(I) The first-target-guided navigation task. In each lap, mice experience the same multisensory environment as in the olfactory-guided and visually-guided navigation tasks, with the only difference being that the reward location is at the first landmark, regardless of the landmark's modality.

(J) Task engagement is quantified by anticipatory behaviors such as pre-reward slowing and increased licking prior to reaching the first landmark, but not in response to the second landmark, irrespective of the landmark's modality, as shown for all sessions. 7 mice; n = 41 sessions; two-tailed Wilcoxon signed-rank test: speed, z(40) = −5.6, p = 2.4e−8; licking, z = 5.5, p = 4.1e−8. *p < 0.05.

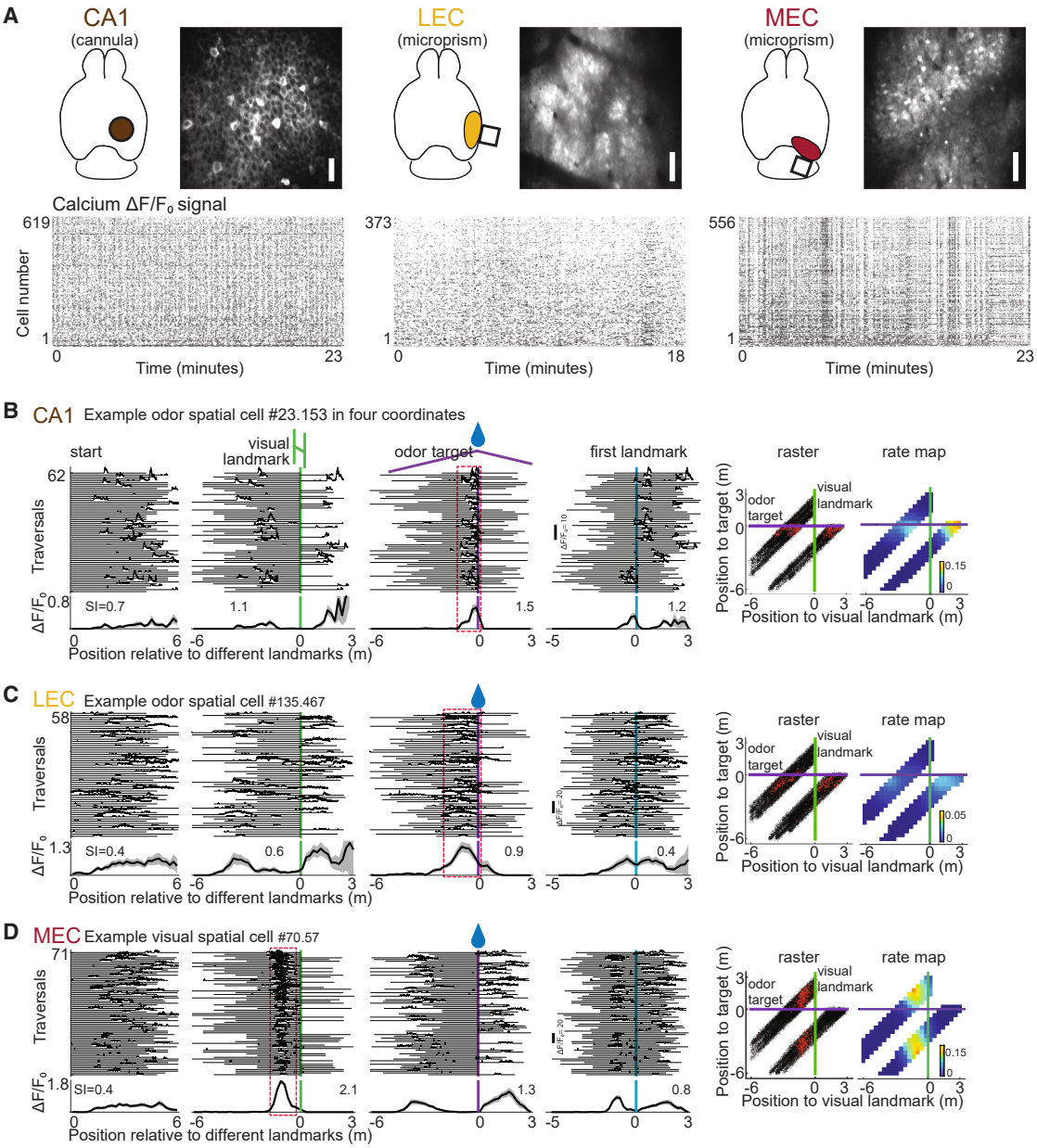

Figure 2. Hippocampal and entorhinal two-photon imaging during multisensory virtual navigation

(A) Left: 2-P imaging of CA1 neurons expressing GCaMP6m through the hippocampal window (top) and $\Delta F/F_0$ versus time traces for CA1 populations in the example session (bottom). Middle: 2-P microprism imaging of LEC neurons expressing GCaMP6s through a microprism. Right: 2-P microprism imaging of MEC neurons expressing GCaMP6s through a microprism. White bars = 50 μm.

(B) Example CA1 odor-spatial cell shown in four coordinates during an olfactory-guided navigation session. Top: Each horizontal trace represents the calcium trace ($\Delta F/F_0$) of the cell in a traversal lap versus the position relative to four different landmarks, i.e., relative to track start (first column), visual landmark (second column), rewarded (blue droplet) odor target (third column), and first landmark (fourth column). Bottom: Average spatial tuning of the example cell relative to four different landmarks. The spatial information (SI) value in each coordinate is shown. Dashed red rectangle shows the tuning field of the example odor-spatial cell. Right: for the example odor spatial cell, the raster plot of the MLE-deconvolved spikes (red dots; STAR Methods) is depicted relative to locations of odor target and visual landmarks. These spikes are overlaid on the animal's position (black dots). The rate map of the raster plot (in Hz) for the example cell is also shown. This example odor spatial cell is active before the odor target regardless of the visual landmark's positions, resulting in a horizontal extent in raster and rate maps.

(C) An example LEC odor-spatial cell shown in four coordinates during an olfactory-guided navigation session.

(D) An example MEC visual-spatial cell shown in four coordinates during an olfactory-guided navigation session.

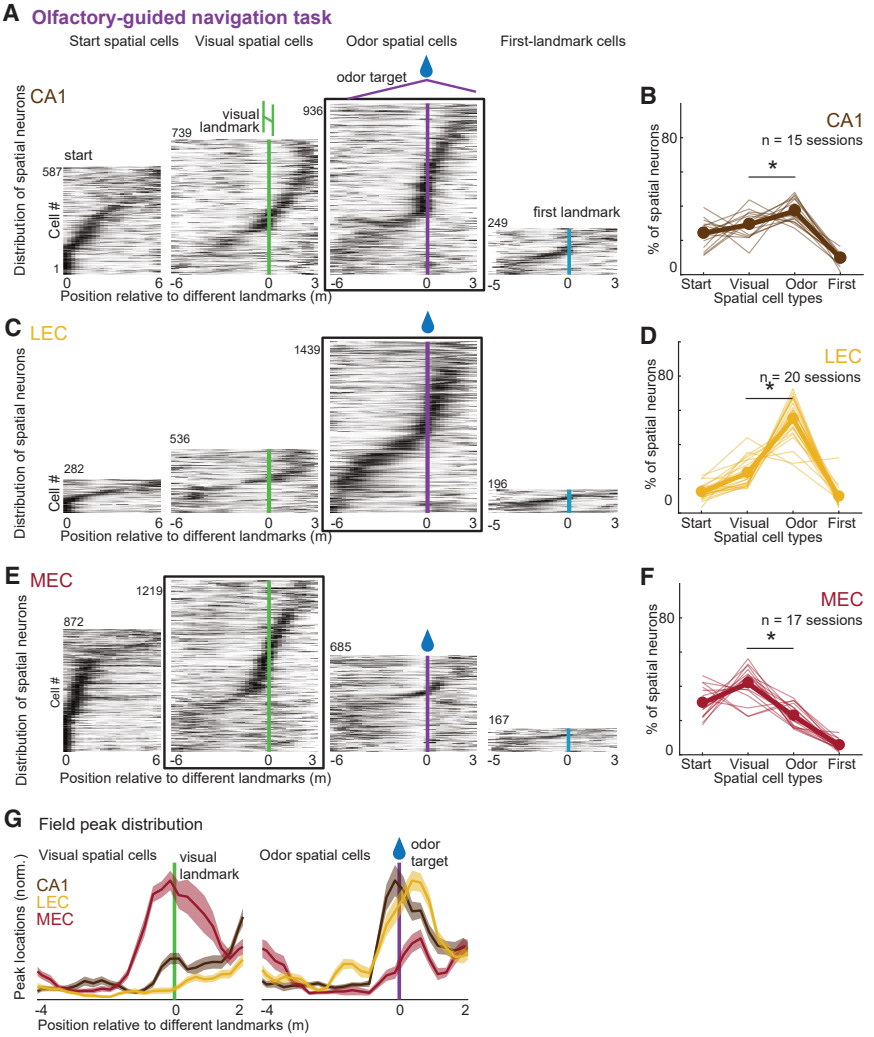

Figure 3. LEC maps olfactory space, and MEC maps visual space during olfactory-guided navigation

(A) All sorted and cross-validated CA1 spatial neurons from all sessions were classified either as start-spatial, visual-spatial, odor-spatial, or first-landmark cells during the olfactory-guided navigation task. Each horizontal line shows the spatial tuning of each spatial neuron. The black box highlights the space most strongly mapped by CA1.

(B) The distribution of four CA1 spatial cell types during olfactory-guided navigation. Each trace shows the fraction of spatial cell types in a session (brown lines); the mean across sessions is shown in thick brown. 3 mice, $n = 15$ sessions, two-tailed Wilcoxon signed-rank test: odor versus start, $p = 8.5e{-}4$; odor versus visual, $p = 0.04$; odor versus first, $p = 6.1e{-}5$. *$p < 0.05$.

(C and D) The populations of LEC spatial cells as described above for CA1. 4 mice, 20 sessions, two-tailed Wilcoxon signed-rank test: odor versus start, $p = 4.4e{-}4$; odor versus visual, $p = 4.4e{-}4$; odor versus first, $p = 4.4e{-}4$.

(E and F) The populations of MEC spatial cells as described above for CA1. 4 mice, 16 sessions, two-tailed Wilcoxon signed-rank test: visual versus start, $p = 0.039$; visual versus odor, $p = 0.0013$; visual versus first, $p = 4.4e{-}4$.

(G) Distribution of spatial field peaks of CA1, LEC, and MEC spatial cell populations. Visual (left) and odor (right) spatial cell peaks are shown relative to visual and odor landmarks.

See also Figures S1 and S2.

In particular, there was robust mapping of the olfactory space, with a larger fraction of cells encoding locations around the rewarded olfactory target (i.e., reward clustering). We also used a separate population analysis method, i.e., Bayesian decoding using all active cells, to investigate how CA1 mapped the different spaces. This analysis provided a similar picture to the above spatial information-based analysis, confirming that CA1 carried information about mouse position relative to each of the landmarks, with the lowest decoding error relative to (and near to) the odor target (Figure S1F). These results establish that CA1 encodes multiple spaces during the olfactory-guided task, with a preference for mapping olfactory space. These findings largely are in line with our previous results of olfactory and visual space mapping in CA1.[17]

In comparison with CA1, in LEC (4 mice, 20 sessions, 5,984 active cells; 299.2 ± 43.3 active cells per session; 37.6% ± 3.0% spatial cells) we found far more pronounced mapping of the olfactory space compared with the other spaces, with spatial cells primarily classified as odor-spatial cells (Figures 2C, 3C, 3D, S1C, and S1E). The heat maps (Figure 3C), along with peak distribution histograms (Figure 3G), revealed that odor spatial cells tiled the full olfactory space. This pattern of tiling is a hallmark of spatial mapping, and is not consistent with early sensory processing since the same odor concentrations on either side of the odor landmark would result in symmetric cell tuning across the landmark (e.g. cells that are active both before and after the landmark, Figure 1B)—a pattern not observed here (see also Figure S2B). Similarly, Bayesian LEC population decoding revealed lower position-decoding error across the olfactory space compared with the visual and other spaces (Figure S1F). These results establish the first evidence that LEC maps an external sensory space and indicate that LEC preferentially maps odor rather than visual spaces in the olfactory-guided navigation task.

In contrast to both CA1 and LEC, in MEC (4 mice, 16 sessions, 4,121 active cells; 257.6 ± 21.7 active cells per session; 57.3% ± 3.26% spatial cells) we found more pronounced mapping of the (distractor) visual space compared with the other spaces, with spatial cells primarily classified as visual-spatial cells (Figures 2D, 3E, 3F, S1C, S1E, and S2C). The heat maps (Figure 3E), along with peak distribution histograms (Figure 3G), revealed that the visual spatial cells largely tiled the full visual space. This pattern of tiling is a hallmark of visual spatial mapping and is not consistent with early sensory encoding of the visual landmark; otherwise, there would be little spatial

tuning once the large archway is passed by the mouse—a pattern not observed here (Figures 1B, 3E, 3G, and S2C). Interestingly, MEC displayed more robust mapping of the track start space compared with LEC, consistent with its known role in path integration.[60,61] Similarly, though MEC contained a population of odor-spatial cells, these cells did not appear to tile the full olfactory space as in LEC, and instead their information appeared to largely derive from decreased firing before the odor target (Figure S1G). This is more consistent with previously described MEC speed cells[62,63] than with olfactory space-mapping cells. Bayesian MEC population decoding analysis revealed a similar story. While the lowest decoding error was observed close to both the visual landmark and odor target, a broader space around the visual landmark had a lower decoding error compared with the odor target (Figure S1G). The region of low decoding error around the odor target is likely due to the speed information mentioned above. These findings establish that MEC primarily maps visual space in the olfactory-guided navigation task, a remarkable contrast with LEC and CA1, particularly given that visual space is not behaviorally relevant during this task.

Altogether, the above results highlight significant and previously unknown differences in how hippocampal and entorhinal cortical regions encode multisensory spaces. While CA1 mapped track start, odor, and visual spaces, there was a preference for mapping olfactory space during the olfactory-guided task. In contrast, LEC preferentially mapped odor, rather than visual, space, and MEC preferentially mapped visual, rather than olfactory space, which can be observed by comparing the proportion of different spatial cell types across brain regions (Figures 3A–3F).

LEC maps olfactory space and MEC visual space during visually-guided navigation

Recent research found differences in CA1 in the encoding of odor and visual spaces depending on behavioral relevance.[17] However, it is unclear whether or how MEC and LEC populations might change based on the behavioral relevance of different sensory modalities. Thus, we used the "visually-guided" navigation task to determine whether our above results are general or task-specific. All aspects of this task were identical to the olfactory-guided task, except that the mice received water rewards only at the visual target location rather than at the odor target location (Figure 1G). Mice (14 mice, n = 65 sessions) robustly performed visually guided navigation with high task engagement (Figures 1H, S3A, and S3B).

We first imaged CA1 (3 mice, 13 sessions, 4,787 active cells; 368.2 ± 23.5 active cells per session; 48% ± 3.2% spatial cells) and found significantly more visual spatial cells than the other three populations, though there was still a small fraction of start spatial cells and very few odor spatial and first-landmark spatial cells (Figures 4A, 4B, S3C, and S3E). The heat maps (Figures 4A and S4A), along with peak distribution histograms of the different CA1 spatial cell populations (Figure 4G), revealed robust mapping of visual space and reward clustering around the visual target. Bayesian population analysis also confirmed that CA1 carried information about mouse position in the visual space, with the lowest decoding error relative to (and near) the visual target (Figure S4F). These results establish that CA1 primarily and preferentially maps visual space during visually-guided multisensory navigation, consistent with our previous findings.[17]

In contrast to CA1, in LEC (5 mice, 19 sessions, 3,412 active cells; 179.6 ± 18.6 active cells per session; 33.7% ± 2.6% spatial cells), we found a pronounced mapping of the (distractor) olfactory space. We found that odor-spatial and visual-spatial cells were the primary spatial cell types, present in similar proportions (Figures 4C, 4D, S3C, and S3E). The heat maps (Figure 4C), along with peak distribution histograms (Figure 4G), revealed that LEC visual-spatial cells exhibited robust reward clustering around the visual target and firing fields before and after the reward, reminiscent of previously described reward experience epochs.[24,26] In contrast, the odor spatial cells tiled the full olfactory space, as seen in the olfactory-guided task. Similarly, Bayesian LEC population decoding revealed relatively broad and homogeneously low decoding error across the olfactory space, and low decoding error only at the rewarded visual target in visual space (Figure S3F). The region of low decoding error around the visual target is likely a result of the reward-experience information mentioned above. These results provide further support for our finding that LEC maps an external sensory space and indicate that, in the visually-guided task, in which the olfactory space was behaviorally irrelevant, LEC still preferentially mapped it. At the same time, LEC neurons encoded aspects of reward experience near the visual target.

In contrast to LEC and similar to CA1, in MEC (6 mice, 32 sessions, 9,360 active cells; 292.5 ± 27.5 active cells per session; 62.1% ± 3.0% spatial cells), we found a pronounced mapping of the visual space compared with the other spaces. We found that visual-spatial cells were the primary spatial cell type (Figures 4E, 4F, S3C, and S3E). The heat maps (Figure 4E), along with peak distribution histograms (Figure 4G), revealed that the visual spatial cells largely tiled the full visual space with some mapping of the start space and little to no mapping of the olfactory and first target spaces. Bayesian MEC population-decoding analysis revealed significantly lower position-decoding error across the visual space and around the rewarded visual target compared with the olfactory space (Figure S3F). The region of low decoding error around the odor target is likely a result of the speed information mentioned above for the olfactory-guided task, but is also present in the visually-guided task, in which a speed increase occurs around the odor target (Figure S3G). These findings establish that MEC primarily maps visual space during visually-guided navigation and provide further support for the idea of a visual space encoding preference in MEC.

Altogether, these results provide further support for our findings of significant and previously unknown differences in how hippocampal and entorhinal cortical regions encode multisensory spaces. In the visually-guided task, MEC preferentially mapped visual space, whereas LEC continued to map olfactory space even though it was not behaviorally relevant. These results were similar to those observed in the olfactory-guided navigation task. CA1, on the other hand, preferentially mapped the visual space in the visually-guided task and the olfactory space in the olfactory-guided task. Thus, our results demonstrate significant task-dependent mapping of the same multisensory environment in CA1, and preferential mapping of specific sensory modalities in MEC and LEC with significantly less task dependence.

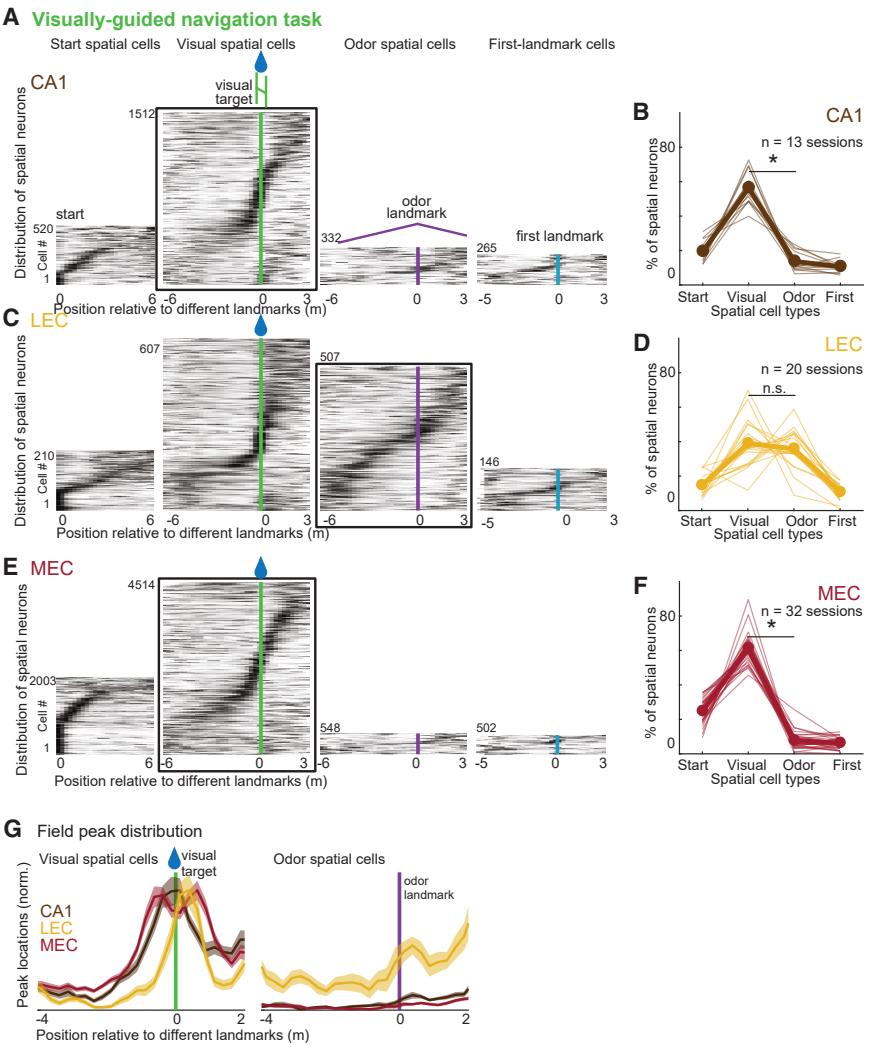

Figure 4. LEC maps olfactory space, and MEC maps visual space during visually-guided navigation

(A and B) All cross-validated and sorted CA1 spatial cell types (A) and their distributions (B). The black box highlights the space most strongly mapped by CA1. Each brown trace shows the fraction of spatial cell types in a session (mean in thick brown trace). 3 mice, 13 sessions; two-tailed Wilcoxon signed-rank test: visual versus start, p = 2.4e−4; visual versus odor, p = 2.4e−4; visual versus first, p = 2.4e−4.

(C and D) All cross-validated and sorted LEC spatial cell types (C) and their distributions (D). 5 mice, 19 sessions; two-tailed Wilcoxon signed-rank test: odor versus start, p = 0.0012; odor versus visual, p = 0.77; odor versus first, p = 2.4e−4.

(E and F) All cross-validated and sorted MEC spatial cell types (E) and their distributions (F). 6 mice, 32 sessions; two-tailed Wilcoxon signed-rank test: visual versus start, p = 3.8e−6; visual versus odor, p = 3.8e−6; visual versus first, p = 3.8e−6.

(G) Distribution of spatial field peaks of CA1, LEC, and MEC spatial cell populations. Visual (left) and odor (right) spatial cell peaks are shown relative to the visual and odor first landmarks.

See also Figures S3 and S4.

CA1, rather than the entorhinal cortex, maps a modality-invariant space

Rodents foraging for visible or odor-emitting hidden food might sometimes rely on an abstract, modality-invariant representation of distance to the nearest food, regardless of whether it is visible or odor-emitting. How the cortico-hippocampal network maps multisensory space, when spatial information from both modalities is required, remains largely unknown. We have previously shown that a subset of CA1 neurons encodes such a modality-invariant "first-target" space.[17] However, it remains unclear whether and how LEC and MEC contribute to encoding this abstract space. We therefore next used the "first-target guided" navigation task. All aspects of this task were identical to the previous two tasks except that the mice received rewards only at the landmark (visual or odor) that appeared first along the track (Figure 1I).

Mice (7 mice, 41 sessions) robustly performed first-target guided navigation with high task engagement (Figures 1J, S5A, and S5B). Imaging CA1 revealed significantly more first-target spatial cells than the other populations, though there was still a significant fraction of start, visual spatial, and odor-spatial cells (3 mice, 16 sessions, 5,366 active cells; 335.4 ± 21.7 active cells per session; 50.5% ± 2.5% spatial cells; Figures 5A, 5B, S5C, and S5E). The heat maps (Figure 5A), along with peak distribution histograms (Figure 5G), revealed robust mapping of the first-target space and reward clustering around the first target. When we separated trials in which the olfactory landmark appeared first (i.e., the rewarded olfactory landmark) from those in which the visual landmark appeared first (i.e., the rewarded visual landmark), we found that the first-target spatial cells tiled the first-target space in both cases (Figure S6A). This was also the case when we separated trials based on the distance between the landmarks (close versus far; Figure S6D). Through Bayesian population analysis, we confirmed that CA1 carried significant information about mouse position in the abstract first-target space, with the lowest decoding error relative to (and near) the first landmark (Figure S5F). These results establish that CA1 preferentially maps the first-target space during first-target guided multisensory navigation, largely in line with our previous findings.[17]

In contrast to CA1, in LEC (2 mice, 13 sessions, 2,538 active cells; 195.2 ± 20.1 active cells per session; 34.4% ± 3.3% spatial cells), we found a pronounced mapping of the olfactory space. We found that odor-spatial cells were the primary spatial cell type, with a notable, though lesser, presence of other cell types (Figures 5C, 5D, S5C, and S5E). The heat maps (Figure 5C), along with peak distribution histograms (Figure 5G), revealed that LEC first target-spatial cells exhibited

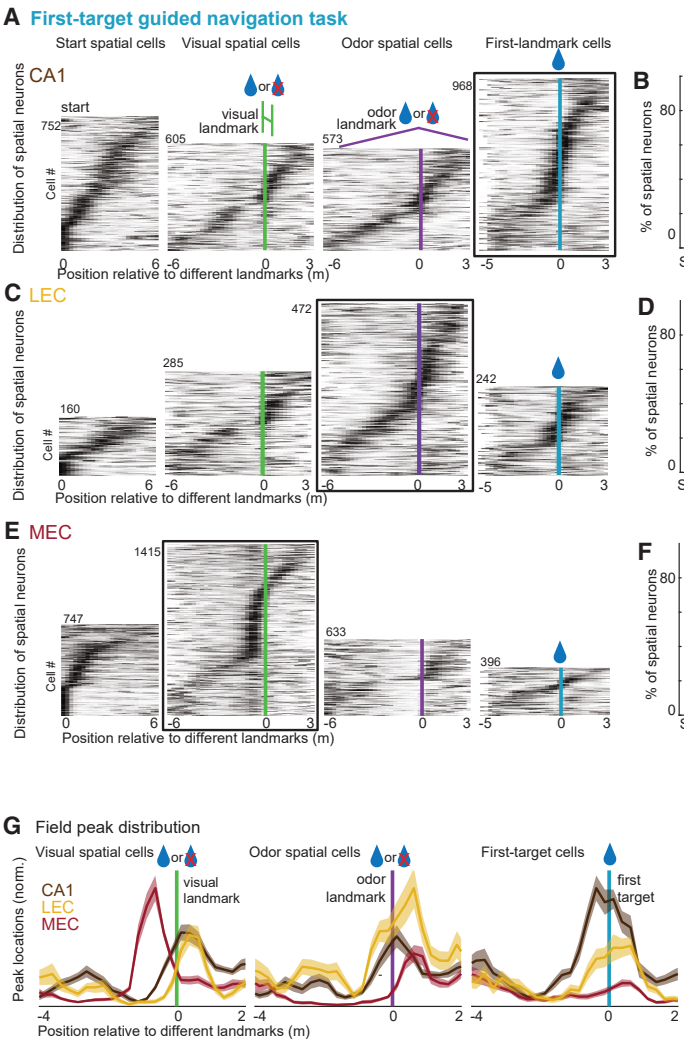

Figure 5. LEC maps olfactory space, and MEC maps visual space during modality-invariant multisensory navigation

(A and B) All cross-validated and sorted CA1 spatial cell types (A) and their distributions (B). While the first target is always rewarded (blue droplet), visual and olfactory landmarks may or may not be rewarded depending on their order of appearance in each traversal lap. The black box highlights the space most strongly mapped by CA1. Each thin gray trace shows the fraction of spatial cell types in a session (mean in thick trace). 3 mice, 16 sessions, two-tailed Wilcoxon signed-rank test: first versus start, $p = 0.044$; first versus visual, $p = 0.039$; first versus odor, $p = 0.034$. $^{*}p < 0.05$.

(C and D) All cross-validated and sorted LEC spatial cell types (C) and their distributions (D). 2 mice, 13 sessions; two-tailed Wilcoxon signed-rank test: odor versus start, $p = 9.8e{-}4$; odor versus visual, $p = 0.0049$; odor versus first, $p = 9.8e{-}4$.

(E and F) All cross-validated and sorted MEC spatial cell types (E) and their distributions (F). 2 mice, 12 sessions, two-tailed Wilcoxon signed-rank test: visual versus start, $p = 0.0024$; visual versus odor, $p = 9.8e{-}4$; visual versus first, $p = 4.9e{-}4$.

(G) Distribution of spatial field peaks of CA1, LEC, and MEC spatial cell populations. Visual (left), odor (middle), and first-target (right) spatial cell peaks are shown relative to visual, odor, and first landmarks.

See also Figures S5 and S6.

robust reward clustering around the first target and broad firing fields before and after the reward, reminiscent of previously described reward experience epochs[24,26] and similar to that observed in the visually-guided task. In contrast, the odor spatial cells tiled the full olfactory space, as seen in the other two tasks. Importantly, separating trials in which the olfactory landmark was first (rewarded) versus second (unrewarded) showed that odor spatial cells tiled olfactory space in both cases (Figure S6B). This was also the case in close versus far landmark trials (Figure S6E). These results further establish LEC's preferential mapping of olfactory space, with evidence of this mapping now in a paradigm that requires abstraction across sensory modalities.

In contrast to both CA1 and LEC, in MEC (2 mice, 12 sessions, 4,450 active cells; 370.8 ± 27.1 active cells per session; 54.3% ± 3.4% spatial cells), we found a pronounced mapping of the visual space. We found that visual-spatial cells were the primary spatial cell type, with a notable, though lesser, presence of other cell types (Figures 5E, 5F, S5C, and S5E). The heat maps (Figure 5E), along with peak distribution histograms (Figure 5G), revealed that the visual spatial cells tiled most of the visual space with more significant reward clustering compared with the two other tasks. Importantly, when we separated trials in which the visual landmark appeared first (i.e., the rewarded visual landmark) from those in which it appeared second (i.e., the unrewarded visual landmark), we found that the visual spatial cells tiled the visual space in both cases (Figure S6C). This was also the case in close versus far landmark trials (Figure S6F). MEC also displayed some mapping of the track start, olfactory, and first target spaces. These results further establish MEC's preferential mapping of visual space.

These findings from the first-target guided navigation task are further supported by population-level analyses. Whereas LEC and MEC exhibited robust mapping of the odor and visual spaces, respectively, CA1 showed a markedly dense mapping of the abstract first-target space (Figures 5G and S6). Additionally, CA1 exhibited the lowest Bayesian population decoding error across the first-target space (Figure S5F). Thus, as in the olfactory-guided and visually-guided navigation tasks, in the first-target task, LEC preferentially mapped the olfactory space, whereas MEC preferentially mapped the visual space. CA1, on the other hand, preferentially mapped the olfactory space in the olfactory-guided task, the visual space in the visually-guided task, and the modality-invariant first target space in the first-target guided task.

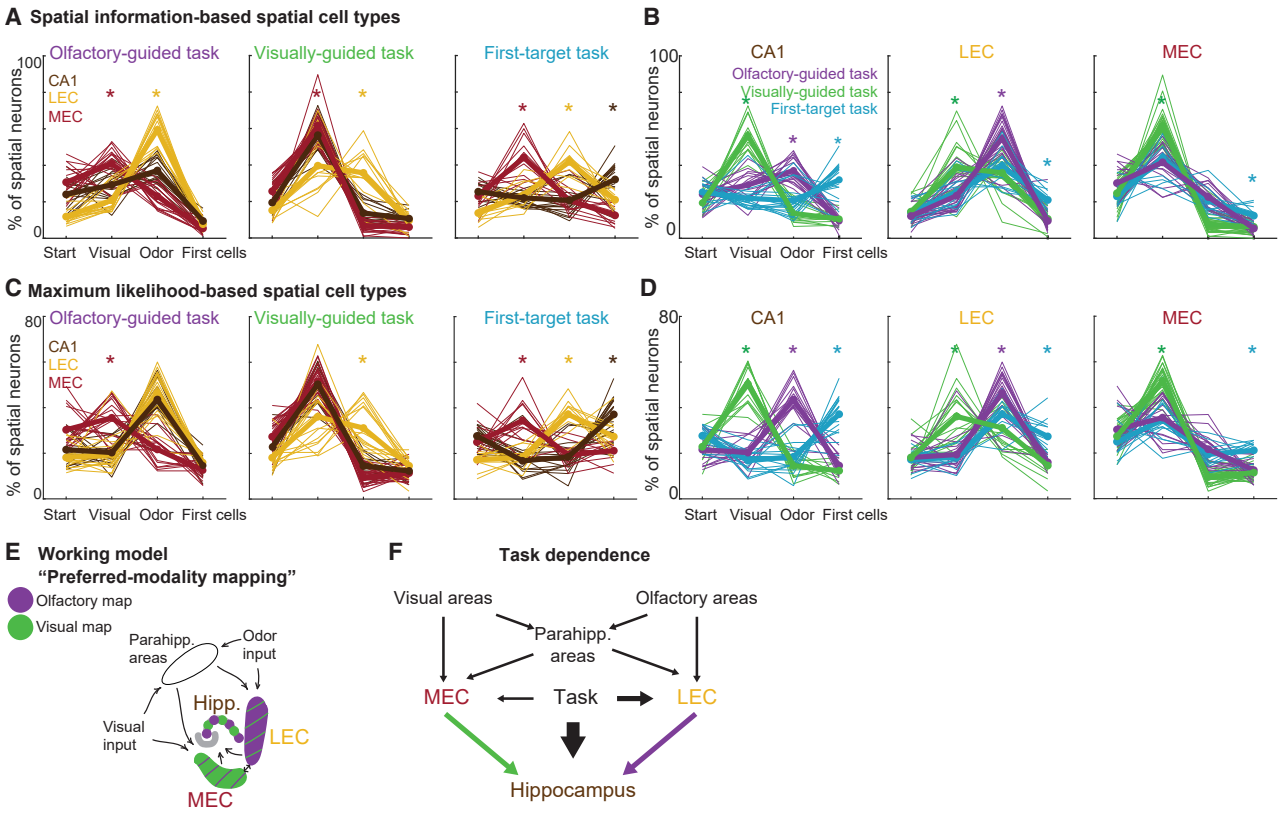

Figure 6. Mapping is sensory modality-specific in the entorhinal cortex and task-specific in CA1

(A) The distribution of four spatial-information-based spatial cell types derived from CA1, LEC, and MEC during olfactory-guided (left), visually-guided (middle), and first-target guided (right) navigation tasks. Each thin trace shows the fraction of spatial cell types in a session (thick lines = mean). The asterisks and their colors indicate cases in which the fraction of a particular cell type is statistically higher ($p < 0.05$) in one brain region compared with the other two. Detailed statistics are reported in Table S1.

(B) The distribution of four spatial-information-based spatial cell types in the three navigation tasks in CA1 (left), LEC (middle), and MEC (right). Each thin trace shows the fraction of spatial cell types in a session (thick lines = mean). The asterisks and their colors indicate cases in which the fraction of a particular cell type is statistically higher ($p < 0.05$) in one task compared with the other two. Detailed statistics are reported in Table S1.

(C) The percentage of MLE-based start, visual, odor, and first-target spatial cells in olfactory-guided (left), visually-guided (middle), and first-target guided (right) tasks. Each thin trace shows a session, with different colors showing different brain regions, and thick colors show the averages of sessions. Detailed statistics are reported in Table S1.

(D) The percentage of the same four MLE-based spatial cell types across tasks for each brain region, including CA1 (left), LEC (middle), and MEC (right), recorded during different multisensory tasks. Detailed statistics are reported in Table S1.

(E) Schematics of the proposed multisensory spatial representation model in the hippocampal-entorhinal network.

(F) A general schematic of spatial sensory pathways and task modulations in the hippocampal-entorhinal network.

See also Figure S7.

Mapping is sensory modality-specific in the entorhinal cortex and task-specific in CA1

To summarize and further quantify our findings, we directly compared the proportion of different cell types across brain regions and tasks (Figure 6A). In the olfactory-guided navigation task, LEC and CA1 preferentially mapped the rewarded olfactory space, whereas MEC preferentially mapped the visual space. In the visually-guided navigation task, CA1 and MEC strongly mapped visual space, whereas LEC continued to map olfactory space, but with reward clustering around the visual target. During the first-target guided navigation task, whereas MEC preferentially mapped the visual space and LEC preferentially mapped the olfactory space, CA1 preferentially mapped the first-target space (Figure 6A; Table S1). Importantly, across the brain regions, we found strikingly different levels of task modulations, as reflected in changes in the proportions of cells mapping the olfactory, visual, and first-target spaces across tasks (Figure 6B; Table S1). CA1 demonstrated dramatic task modulation: its neural population primarily mapped the behaviorally relevant space, i.e., olfactory space in the olfactory-guided task, visual space in the visually-guided task, and the abstract first-target space in the first-target guided task. In contrast to CA1, LEC and MEC displayed far less task modulation, with LEC and MEC preserving their preferences for mapping olfactory and visual spaces across the three tasks, respectively, with only some modulations in the fractions of cell types based on the behavioral relevance of the space (Figure 6B).

To further verify our findings, we used a third independent method (in addition to the Information and Bayesian analyses), the maximum likelihood estimation (MLE) framework (STAR Methods). We chose this method because our spatial information-based method does not consider conjunctive spatial tunings of individual cells, for example, a cell with significant information in both visual and olfactory reference frames, but the MLE framework allowed us to quantify any such conjunctivity. For this analysis, we quantified the cross-validated goodness-of-fit of each cell's response in all possible spaces, including conjunctive spaces between two spatial coordinates (Figures S7A–S7C; STAR Methods). Of the total 45,277 recorded active cells across different brain regions and tasks, 21,909 (48.8%) were identified as spatial cells using our MLE approach, of which 84.2% were classified as pure (non-conjunctive) start, visual, odor, and first-target spatial cell types (Figure S7D). We examined the proportion of these MLE-identified, four non-conjunctive cell type populations and found that their distributions across brain regions and navigation tasks were highly similar to those revealed by our spatial information-based classification (Figures 6C and 6D; Table S1). We did, however, identify some conjunctive spatial processing across different brain areas and tasks, with these spatial cells (i.e., the remaining 15.8% of spatial cells) identified as conjunctive start-visual, start-odor, start-first, and visual-odor spatial cells; these cells are described in supplemental data (Figures S7E–S7H). Thus, even with an MLE analysis approach capable of examining conjunctivity, the vast majority of active cells predominantly encoded one of our four previously defined spaces (i.e., start, visual, odor, or first-target) and, importantly, the distribution of these cells across brain regions and tasks confirmed our above key results.

We therefore established, using multiple independent analytical methods, that behavior significantly modulates the mapping of multisensory space in CA1, whereas the entorhinal cortex largely maintains preferential and modality-specific mapping despite changes in behavior. Thus, we propose a new working model of multisensory mapping in the entorhinal cortex, the ''preferred-modality mapping'' model, in which MEC and LEC predominantly represent visual and olfactory spaces, respectively, with a smaller fraction of cells in each region responding to the other sensory modality and significantly less behavioral modulation compared with CA1 (Figures 6E and 6F). In this framework, CA1 may use modality-preferred spatial maps from its upstream entorhinal inputs to perform flexible, and if required, modality-invariant computations necessary for multisensory navigation.

DISCUSSION

While olfaction is traditionally considered a contextual cue due to the perception that it is slowly changing or carries little spatial information, many studies have found a role for olfactory-guided navigation across many species.[4,52,53,64–66] Indeed, the sense of olfaction contains significant spatial information, comparable in many cases with the sense of vision,[67,68] and animals are capable of rapid, sub-sniff-rate odor detection to support olfactory-guided navigation.[69] While place-related activity has been observed in the olfactory bulb[70] and the piriform cortex,[30,71] a brain region that maps the full olfactory space of an animal's local environment during navigation had not yet been identified. Our findings establish LEC as such a region that robustly maps the olfactory space across different behavioral contexts. LEC receives direct input from both the olfactory bulb[72,73] and the piriform cortex,[74,75] and is known to be modulated by these regions.[76–78] We speculate that primary olfactory sensory inputs are conveyed from these regions to the LEC, in which this information may be combined with self-motion signals to form the spatial map of olfactory space that we observed. Components of this spatial map may then be transmitted from LEC back to the olfactory bulb and piriform cortex, accounting for the previous observations of their place-related activity. Notably, this olfactory mapping represents the first clear evidence of any spatial map in LEC. LEC neurons were previously shown to encode non-spatial, or egocentric, spatial information,[22,23,31–35] and they have been implicated in processing reward.[24–26] Our results add spatial mapping of olfactory spaces to this list for LEC and lead to the question of how one region encodes so many different variables related to behavior. One possibility is that LEC consists of many distinct, parallel circuits, each supporting the encoding of different representational domains. Indeed, consistent with this idea, we observed, in addition to a map of olfactory space, reward-related encoding.

MEC, on the other hand, has been extensively implicated in visual spatial coding,[36–40,45–48,57,62,79,80] visual cue processing,[49,81] as well as in encoding reward,[82–84] time,[85,86] and cognitive spaces such as sound.[87,88] Recent studies have demonstrated audiovisual sensory integration in MEC,[88] and have shown that MEC activity is more disrupted by visual than tactile deprivation.[89] However, the capacity of MEC to map olfactory space, or to perform olfactory-visual spatial integration, remained unknown. This question is of particular interest given that MEC does receive input from the piriform cortex.[19] Here, we found that MEC consistently mapped visual rather than olfactory space, even when vision was not behaviorally relevant, and with only minor task-related modulation. A small subset of MEC neurons in the olfactory-guided navigation task was classified as odor spatial cells, but closer inspection suggests that these were largely speed cells or speed-modulated grid cells (Figure S1G),[62,63] whose activity decreased as animals slowed before reaching the rewarded odor target. While grid cells in MEC have traditionally been assumed to map multisensory spaces,[36–38] our results bring up the intriguing possibility that grid cells may predominantly map spaces defined by visual landmarks. However, our findings here come from spatially tuned neurons in 1-dimensional tracks (not necessarily grid cells), and so more research will be required to more clearly determine the sensory modality preferences of grid cells in 2-D spaces.[36] Indeed, future studies using 2-D multisensory environments may also be able to determine the properties of the olfactory space map we identified in LEC, in which we speculate that grid cells tiling 2D olfactory space may exist.

We found that behavioral demand modulates spatial representations in both LEC and MEC, though significantly less than in CA1 (Figure 6). In the entorhinal cortices, these modulations were largely attributable to non-spatial encoding dimensions, such as speed dependence and reward encoding, which are

shaped by the animal's behavior. The encoding of these nonspatial dimensions provides a likely explanation for nonpreferred modality encoding in MEC and LEC, particularly in our Bayesian decoding analysis (Figures S1F, S3F, and S5F). For example, in MEC, the region of low decoding error around the odor target in the odor-guided task is likely a result of speed-coding neurons combined with the animal changing speed around the odor target (Figure S1F). In LEC, the region of low decoding error around the visual target in the visual-guided task is likely a result of reward-experience coding neurons (Figure S3F).

Nonetheless, our analyses suggest that a small fraction of spatial cells in LEC and MEC genuinely encode sensory spaces other than their preferred modalities (see example cells in Figures S1E, S3E, and S5E). Such visual spatial tuning in LEC or olfactory spatial tuning in MEC could arise from feedback projections from the hippocampus. Indeed, the entorhinal-hippocampal network is structured as a recurrent loop, with the hippocampus, via the subiculum, projecting back to both the LEC and the MEC,[90,91] and likely contributing to the emergence of some cross-modality representations. For example, LEC receives spatially tuned input from both CA1[92] and MEC,[21] and hippocampal feedback activates MEC in response to olfactory stimuli.[93] These feedback pathways may underlie the occasional presence of spatial cells encoding non-preferred modalities in LEC and MEC observed here. Alternatively, LEC and MEC do receive some input from visual and olfactory cortical regions, respectively,[19] which could account for such cross-modal spatial coding. Further, such cross-modal spatial coding may arise through processing in parahippocampal regions that project to MEC and LEC, including the perirhinal and postrhinal cortices or the claustrum, which have been implicated in multisensory spatial integration.[21,94–96] For example, LEC receives spatially tuned input from the postrhinal cortex.[97]

Modality-invariant cognition has a neural basis in the hippocampus. For example, single neurons in the human hippocampus and, rarely, in the entorhinal cortex, invariantly represent both the face and written name of an individual,[98] defining the existence of "concept cells" in the entorhinal-hippocampal network.[99,100] Similarly, we found that modality-invariant abstract space mapping appears to be mostly formed in the hippocampus. This comes from our finding that LEC and MEC perform modality-dependent spatial mappings, respectively mapping olfactory and visual spaces, and the hippocampus appears to integrate these modality-dependent spatial inputs to build higher-level modality-invariant maps for multisensory navigation. These findings provide insight into how abstract representations might be constructed in the hippocampus,[101–103] supporting the idea that the hippocampus is able to select the necessary components to build such spaces from separate, parallel representations in presynaptic regions.

These ideas fit into a long history of literature describing parallel information streams from MEC and LEC that are integrated in the hippocampus.[104,105] In the classic model, spatial signals travel through the MEC, whereas nonspatial signals pass through the LEC, and the two streams converge in the hippocampus to construct a context-dependent cognitive map.[20,21,106,107] In one application of this idea,[108] nonspatial information about objects or cues could be sent to the hippocampus through the LEC, in which it is combined with spatial information from the MEC to produce conjunctive object-place representations.[106] Indeed, information about the location of objects can be found in LEC, largely in the form of egocentric bearing information.[22] This brings up the question of whether or how such object-bearing cells might be related to the olfactory spatial representations described here. A reasonable possibility is that the objects used in this prior study each had unique odors, and thus odor cues could have been used to build a bearing representation with respect to the objects. It will be interesting for future studies to explore whether such a bearing representation, combined with idiothetic cues, could form the basis for mapping 2D odor spaces, such as our speculation above about LEC grid cells.

Our results, along with recent studies, support the hippocampus's role in generating goal-directed spatial representations for action planning.[18] Indeed, in many cases, hippocampal activity primarily encodes space relative to reward,[109] and its output provides essential information to prefrontal circuits for constructing goal-directed behavioral frameworks.[110] Our study suggests that a key to this ability of the hippocampus in generating flexible, goal-directed, multisensory cognitive maps arises from its selective inheritance of entorhinal modality-specific spatial maps.

Limitations of the study

Our study focused specifically on the spatial representations of olfactory and visual modalities, while other sensory modalities were not examined. To minimize external auditory cues, we masked sound using high-volume white noise during experiments. Additionally, mice were not provided with spatially varying tactile cues for whisker sensing. However, both audition[88,110–113] and touch[114,115] are spatial modalities that rodents use during navigation. Future studies should explore how these senses contribute to spatial representations in diverse multisensory navigation tasks.

We used a linearly increasing and decreasing spatial profile for odorant concentration. However, more ethologically valid odor plume dynamics may influence olfactory spatial representations in the brain.[2,116] Future studies may further investigate the impact of odor dynamics and spatial profiles on entorhinal-hippocampal maps. Further, during our imaging experiments, we mainly sampled dorsal regions and superficial layers of LEC and MEC. Therefore, our findings about entorhinal function introduced here are not yet fully generalizable to the entire LEC and MEC regions and their different cortical sublayers.

It would further be informative to determine whether the same LEC or MEC cells are dedicated to encoding olfactory or visual spaces across tasks. However, in our experimental design, we did not investigate this because we did not train mice to switch between two tasks, e.g., the olfactory-guided task and then the visually-guided task, in one experimental session while imaging the same cells over the two tasks. We have previously shown that CA1 spatial cells exhibit global remapping when mice switch between olfactory-guided and visually-guided tasks,[17] with the sensory spatial-mapping identity of cells in the former task not predictive of their identity in the latter. However, the fraction of CA1 visual and olfactory spatial cells is fully modulated in these two tasks, requiring remapping within the modality-dependent

place codes of individual cells. In contrast, LEC and MEC preserve their preferred modality-specific mapping across different tasks; thus, we predict that the encoding preference of individual cells would be preserved across these tasks. Nevertheless, future work will be needed to further explore this question.

RESOURCE AVAILABILITY

Lead contact

Requests for further information and resources should be directed to the lead contact, Daniel A. Dombeck (d-dombeck@northwestern.edu).

Materials availability

This study did not generate new unique reagents.

Data and code availability

- All original imaging data reported in this paper will be shared by the lead contact upon request.
- All original code and processed imaging data have been deposited at Zenodo at https://zenodo.org/records/18734619 (DOI: https://doi.org/10.5281/zenodo.18734619) and are publicly available as of the date of publication.
- Any additional information required to reanalyze the data reported in this paper is available from the lead contact upon request.

ACKNOWLEDGMENTS

We thank T. Bozza and members of the Dombeck Lab for comments on the manuscript. This work was supported by NIH grants R01MH101297 (D.A.D.), F32NS116023 (H.D.), and T32AG020506 (J.R.C.); and a NARSAD Young Investigator Grant from the Brain and Behavior Research Foundation (J.B.I.). The funders had no role in study design, data collection and analysis, decision to publish, or preparation of the manuscript.

AUTHOR CONTRIBUTIONS

H.D. and D.A.D. planned and designed the experiments. H.D. and J.B.I. performed hippocampal and entorhinal surgeries, respectively. H.D. performed experiments and collected data. H.D. and J.R.C. analyzed the data with help from J.B.I. and D.A.D. H.D. and D.A.D. wrote the paper with inputs and edits from J.R.C. and J.B.I. D.A.D. supervised all aspects of the project.

DECLARATION OF INTERESTS

D.A.D. has a US patent (#11092979) for the olfactory VR technology.

STAR★METHODS

Detailed methods are provided in the online version of this paper and include the following:

- KEY RESOURCES TABLE
- EXPERIMENTAL MODEL AND STUDY PARTICIPANT DETAILS
  - Mice
- METHOD DETAILS
  - Multisensory Virtual Reality (VR) apparatus
  - CA1 surgery
  - LEC surgery
  - MEC surgery
  - Behavior
  - Two-photon imaging
- QUANTIFICATION AND STATISTICAL ANALYSIS
  - Statistics and reproducibility
  - Behavioral analysis
  - Calcium Imaging analysis
  - Spatial information calculation and spatial cell type classification
  - Bayesian reconstruction
  - Maximum likelihood estimation (MLE) for conjunctivity analysis
  - "AND" and "OR" conjunctive cell identification

SUPPLEMENTAL INFORMATION

Supplemental information can be found online at https://doi.org/10.1016/j.neuron.2026.03.008.

Received: September 15, 2025
Revised: January 5, 2026
Accepted: March 4, 2026
Published: March 31, 2026

REFERENCES

1. Tolman, E.C. (1948). Cognitive maps in rats and men. Psychol. Rev. *55*, 189–208. https://doi.org/10.1037/h0061626.
2. Jacobs, L.F. (2012). From chemotaxis to the cognitive map: the function of olfaction. Proc. Natl. Acad. Sci. USA *109*, 10693–10700. https://doi.org/10.1073/pnas.1201880109.
3. Bates, S.L., and Wolbers, T. (2014). How cognitive aging affects multisensory integration of navigational cues. Neurobiol. Aging *35*, 2761–2769. https://doi.org/10.1016/j.neurobiolaging.2014.04.003.
4. Aboitiz, F., and Montiel, J.F. (2015). Olfaction, navigation, and the origin of isocortex. Front. Neurosci. *9*, 402. https://doi.org/10.3389/fnins.2015.00402.
5. Epstein, R.A., Patai, E.Z., Julian, J.B., and Spiers, H.J. (2017). The cognitive map in humans: spatial navigation and beyond. Nat. Neurosci. *20*, 1504–1513. https://doi.org/10.1038/nn.4656.
6. Behrens, T.E.J., Muller, T.H., Whittington, J.C.R., Mark, S., Baram, A.B., Stachenfeld, K.L., and Kurth-Nelson, Z. (2018). What Is a Cognitive Map? Organizing Knowledge for Flexible Behavior. Neuron *100*, 490–509. https://doi.org/10.1016/j.neuron.2018.10.002.
7. Whittington, J.C.R., McCaffary, D., Bakermans, J.J.W., and Behrens, T.E.J. (2022). How to build a cognitive map. Nat. Neurosci. *25*, 1257–1272. https://doi.org/10.1038/s41593-022-01153-y.
8. Igarashi, K.M., Lee, J.Y., and Jun, H. (2022). Reconciling neuronal representations of schema, abstract task structure, and categorization under cognitive maps in the entorhinal-hippocampal-frontal circuits. Curr. Opin. Neurobiol. *77*, 102641. https://doi.org/10.1016/j.conb.2022.102641.
9. Bruns, P., and Röder, B. (2023). Development and experience-dependence of multisensory spatial processing. Trends Cogn. Sci. *27*, 961–973. https://doi.org/10.1016/j.tics.2023.04.012.
10. O'Keefe, J., and Dostrovsky, J. (1971). The hippocampus as a spatial map. Preliminary evidence from unit activity in the freely-moving rat. Brain Res. *34*, 171–175. https://doi.org/10.1016/0006-8993(71)90358-1.
11. O'Keefe, J., and Nadel, L. (1978). The Hippocampus as a Cognitive Map (The Hippocampus as a Cognitive Map) (Oxford University Press).
12. Wood, E.R., Dudchenko, P.A., and Eichenbaum, H. (1999). The global record of memory in hippocampal neuronal activity. Nature *397*, 613–616. https://doi.org/10.1038/17605.
13. Zhang, S., and Manahan-Vaughan, D. (2015). Spatial olfactory learning contributes to place field formation in the hippocampus. Cereb. Cortex *25*, 423–432. https://doi.org/10.1093/cercor/bht239.
14. Fischler-Ruiz, W., Clark, D.G., Joshi, N.R., Devi-Chou, V., Kitch, L., Schnitzer, M., Abbott, L.F., and Axel, R. (2021). Olfactory landmarks and path integration converge to form a cognitive spatial map. Neuron *109*, 4036–4049.e5. https://doi.org/10.1016/j.neuron.2021.09.055.
15. Anderson, M.I., and Jeffery, K.J. (2003). Heterogeneous modulation of place cell firing by changes in context. J. Neurosci. *23*, 8827–8835. https://doi.org/10.1523/JNEUROSCI.23-26-08827.2003.

16. Eichenbaum, H. (2017). The role of the hippocampus in navigation is memory. J. Neurophysiol. *117*, 1785–1796. https://doi.org/10.1152/jn.00005.2017.

17. Radvansky, B.A., Oh, J.Y., Climer, J.R., and Dombeck, D.A. (2021). Behavior determines the hippocampal spatial mapping of a multisensory environment. Cell Rep. *36*, 109444. https://doi.org/10.1016/j.celrep.2021.109444.

18. Zutshi, I., Apostolelli, A., Yang, W., Zheng, Z.S., Dohi, T., Balzani, E., Williams, A.H., Savin, C., and Buzsáki, G. (2025). Hippocampal neuronal activity is aligned with action plans. Nature *639*, 153–161. https://doi.org/10.1038/s41586-024-08397-7.

19. Burwell, R.D., and Amaral, D.G. (1998). Perirhinal and postrhinal cortices of the rat: interconnectivity and connections with the entorhinal cortex. J. Comp. Neurol. *391*, 293–321. https://doi.org/10.1002/(SICI)1096-9861(19980216)391:3<293::AID-CNE2>3.0.CO;2-X.

20. Witter, M.P., Doan, T.P., Jacobsen, B., Nilssen, E.S., and Ohara, S. (2017). Architecture of the Entorhinal Cortex A Review of Entorhinal Anatomy in Rodents with Some Comparative Notes. Front. Syst. Neurosci. *11*, 46. https://doi.org/10.3389/fnsys.2017.00046.

21. Nilssen, E.S., Doan, T.P., Nigro, M.J., Ohara, S., and Witter, M.P. (2019). Neurons and networks in the entorhinal cortex: A reappraisal of the lateral and medial entorhinal subdivisions mediating parallel cortical pathways. Hippocampus *29*, 1238–1254. https://doi.org/10.1002/hipo.23145.

22. Wang, C., Chen, X., Lee, H., Deshmukh, S.S., Yoganarasimha, D., Savelli, F., and Knierim, J.J. (2018). Egocentric coding of external items in the lateral entorhinal cortex. Science *362*, 945–949. https://doi.org/10.1126/science.aau4940.

23. Deshmukh, S.S., and Knierim, J.J. (2011). Representation of non-spatial and spatial information in the lateral entorhinal cortex. Front. Behav. Neurosci. *5*, 69. https://doi.org/10.3389/fnbeh.2011.00069.

24. Issa, J.B., Radvansky, B.A., Xuan, F., and Dombeck, D.A. (2024). Lateral entorhinal cortex subpopulations represent experiential epochs surrounding reward. Nat. Neurosci. *27*, 536–546. https://doi.org/10.1038/s41593-023-01557-4.

25. Jun, H., Lee, J.Y., Bleza, N.R., Ichii, A., Donohue, J.D., and Igarashi, K.M. (2024). Prefrontal and lateral entorhinal neurons co-dependently learn item-outcome rules. Nature *633*, 864–871. https://doi.org/10.1038/s41586-024-07868-1.

26. Bowler, J.C., and Losonczy, A. (2023). Direct cortical inputs to hippocampal area CA1 transmit complementary signals for goal-directed navigation. Neuron *111*, 4071–4085.e6. https://doi.org/10.1016/j.neuron.2023.09.013.

27. Igarashi, K.M., Lu, L., Colgin, L.L., Moser, M.-B., and Moser, E.I. (2014). Coordination of entorhinal-hippocampal ensemble activity during associative learning. Nature *510*, 143–147. https://doi.org/10.1038/nature13162.

28. Li, Y., Xu, J., Liu, Y., Zhu, J., Liu, N., Zeng, W., Huang, N., Rasch, M.J., Jiang, H., Gu, X., et al. (2017). A distinct entorhinal cortex to hippocampal CA1 direct circuit for olfactory associative learning. Nat. Neurosci. *20*, 559–570. https://doi.org/10.1038/nn.4517.

29. Liu, P., Gao, C., Wu, J., Wu, T., Zhang, Y., Liu, C., Sun, C., and Li, A. (2023). Negative valence encoding in the lateral entorhinal cortex during aversive olfactory learning. Cell Rep. *42*, 113204. https://doi.org/10.1016/j.celrep.2023.113204.

30. Mena, W., Baker, K., Rubin, A., Kohli, S., Yoo, Y., Bathellier, B., Ziv, Y., Rezaei-Mazinani, S., and Fleischmann, A. (2025). Differential encoding of odor and place in mouse piriform and entorhinal cortex. Neuro *12*. https://doi.org/10.1523/ENEURO.0026-25.2025.

31. Keene, C.S., Bladon, J., McKenzie, S., Liu, C.D., O'Keefe, J., and Eichenbaum, H. (2016). Complementary Functional Organization of Neuronal Activity Patterns in the Perirhinal, Lateral Entorhinal, and Medial Entorhinal Cortices. J. Neurosci. *36*, 3660–3675. https://doi.org/10.1523/JNEUROSCI.4368-15.2016.

32. Wilson, D.I.G., Watanabe, S., Milner, H., and Ainge, J.A. (2013). Lateral entorhinal cortex is necessary for associative but not nonassociative recognition memory. Hippocampus *23*, 1280–1290. https://doi.org/10.1002/hipo.22165.

33. Wilson, D.I.G., Langston, R.F., Schlesiger, M.I., Wagner, M., Watanabe, S., and Ainge, J.A. (2013). Lateral entorhinal cortex is critical for novel object-context recognition. Hippocampus *23*, 352–366. https://doi.org/10.1002/hipo.22095.

34. Vandrey, B., Garden, D.L.F., Ambrozova, V., McClure, C., Nolan, M.F., and Ainge, J.A. (2020). Fan Cells in Layer 2 of the Lateral Entorhinal Cortex Are Critical for Episodic-like Memory. Curr. Biol. *30*, 169–175.e5. https://doi.org/10.1016/j.cub.2019.11.027.

35. Huang, X., Schlesiger, M.I., Barriuso-Ortega, I., Leibold, C., MacLaren, D.A.A., Bieber, N., and Monyer, H. (2023). Distinct spatial maps and multiple object codes in the lateral entorhinal cortex. Neuron *111*, 3068–3083.e7. https://doi.org/10.1016/j.neuron.2023.06.020.

36. Hafting, T., Fyhn, M., Molden, S., Moser, M.-B., and Moser, E.I. (2005). Microstructure of a spatial map in the entorhinal cortex. Nature *436*, 801–806. https://doi.org/10.1038/nature03721.

37. Høydal, Ø.A., Skytøen, E.R., Andersson, S.O., Moser, M.-B., and Moser, E.I. (2019). Object-vector coding in the medial entorhinal cortex. Nature *568*, 400–404. https://doi.org/10.1038/s41586-019-1077-7.

38. Tukker, J.J., Beed, P., Brecht, M., Kempter, R., Moser, E.I., and Schmitz, D. (2022). Microcircuits for spatial coding in the medial entorhinal cortex. Physiol. Rev. *102*, 653–688. https://doi.org/10.1152/physrev.00042.2020.

39. Sargolini, F., Fyhn, M., Hafting, T., McNaughton, B.L., Witter, M.P., Moser, M.-B., and Moser, E.I. (2006). Conjunctive representation of position, direction, and velocity in entorhinal cortex. Science *312*, 758–762. https://doi.org/10.1126/science.1125572.

40. Solstad, T., Boccara, C.N., Kropff, E., Moser, M.-B., and Moser, E.I. (2008). Representation of geometric borders in the entorhinal cortex. Science *322*, 1865–1868. https://doi.org/10.1126/science.1166466.

41. Pérez-Escobar, J.A., Kornienko, O., Latuske, P., Kohler, L., and Allen, K. (2016). Visual landmarks sharpen grid cell metric and confer context specificity to neurons of the medial entorhinal cortex. eLife *5*, e16937. https://doi.org/10.7554/eLife.16937.

42. Chen, G., Manson, D., Cacucci, F., and Wills, T.J. (2016). Absence of Visual Input Results in the Disruption of Grid Cell Firing in the Mouse. Curr. Biol. *26*, 2335–2342. https://doi.org/10.1016/j.cub.2016.06.043.

43. Waaga, T., Agmon, H., Normand, V.A., Nagelhus, A., Gardner, R.J., Moser, M.-B., Moser, E.I., and Burak, Y. (2022). Grid-cell modules remain coordinated when neural activity is dissociated from external sensory cues. Neuron *110*, 1843–1856.e6. https://doi.org/10.1016/j.neuron.2022.03.011.

44. Wen, J.H., Sorscher, B., Aery Jones, E.A., Ganguli, S., and Giocomo, L.M. (2024). One-shot entorhinal maps enable flexible navigation in novel environments. Nature *635*, 943–950. https://doi.org/10.1038/s41586-024-08034-3.

45. Killian, N.J., Jutras, M.J., and Buffalo, E.A. (2012). A map of visual space in the primate entorhinal cortex. Nature *491*, 761–764. https://doi.org/10.1038/nature11587.

46. Meister, M.L.R., and Buffalo, E.A. (2018). Neurons in Primate Entorhinal Cortex Represent Gaze Position in Multiple Spatial Reference Frames. J. Neurosci. *38*, 2430–2441. https://doi.org/10.1523/JNEUROSCI.2432-17.2018.

47. Wilming, N., König, P., König, S., and Buffalo, E.A. (2018). Entorhinal cortex receptive fields are modulated by spatial attention, even without movement. eLife *7*, e31745. https://doi.org/10.7554/eLife.31745.

48. Kinkhabwala, A.A., Gu, Y., Aronov, D., and Tank, D.W. (2020). Visual cue-related activity of cells in the medial entorhinal cortex during navigation in virtual reality. eLife *9*, e43140. https://doi.org/10.7554/eLife.43140.

49. Wang, G., Shahid, F., Malone, T., Tyan, J., Cekada, K., and Gu, Y. (2025). The entorhinal spatial map integrates visual identity information of landmarks. Preprint at bioRxiv. https://doi.org/10.1101/2025.03.13.643169.

50. Radvansky, B.A., and Dombeck, D.A. (2018). An olfactory virtual reality system for mice. Nat. Commun. *9*, 839. https://doi.org/10.1038/s41467-018-03262-4.

51. Climer, J.R., Davoudi, H., Oh, J.Y., and Dombeck, D.A. (2025). Hippocampal representations drift in stable multisensory environments. Nature *645*, 457–465. https://doi.org/10.1038/s41586-025-09245-y.

52. Gire, D.H., Kapoor, V., Arrighi-Allisan, A., Seminara, A., and Murthy, V.N. (2016). Mice Develop Efficient Strategies for Foraging and Navigation Using Complex Natural Stimuli. Curr. Biol. *26*, 1261–1273. https://doi.org/10.1016/j.cub.2016.03.040.

53. Findley, T.M., Wyrick, D.G., Cramer, J.L., Brown, M.A., Holcomb, B., Attey, R., Yeh, D., Monasevitch, E., Nouboussi, N., Cullen, I., et al. (2021). Sniff-synchronized, gradient-guided olfactory search by freely moving mice. eLife *10*, e58523. https://doi.org/10.7554/eLife.58523.

54. Ackels, T., Erskine, A., Dasgupta, D., Marin, A.C., Warner, T.P.A., Tootoonian, S., Fukunaga, I., Harris, J.J., and Schaefer, A.T. (2021). Fast odour dynamics are encoded in the olfactory system and guide behaviour. Nature *593*, 558–563. https://doi.org/10.1038/s41586-021-03514-2.

55. Baker, K.L., Dickinson, M., Findley, T.M., Gire, D.H., Louis, M., Suver, M.P., Verhagen, J.V., Nagel, K.I., and Smear, M.C. (2018). Algorithms for Olfactory Search across Species. J. Neurosci. *38*, 9383–9389. https://doi.org/10.1523/JNEUROSCI.1668-18.2018.

56. Dombeck, D.A., Harvey, C.D., Tian, L., Looger, L.L., and Tank, D.W. (2010). Functional imaging of hippocampal place cells at cellular resolution during virtual navigation. Nat. Neurosci. *13*, 1433–1440. https://doi.org/10.1038/nn.2648.

57. Heys, J.G., Rangarajan, K.V., and Dombeck, D.A. (2014). The functional micro-organization of grid cells revealed by cellular-resolution imaging. Neuron *84*, 1079–1090. https://doi.org/10.1016/j.neuron.2014.10.048.

58. McKenzie, S., Frank, A.J., Kinsky, N.R., Porter, B., Rivière, P.D., and Eichenbaum, H. (2014). Hippocampal representation of related and opposing memories develop within distinct, hierarchically organized neural schemas. Neuron *83*, 202–215. https://doi.org/10.1016/j.neuron.2014.05.019.

59. Pastalkova, E., Itskov, V., Amarasingham, A., and Buzsáki, G. (2008). Internally generated cell assembly sequences in the rat hippocampus. Science *321*, 1322–1327. https://doi.org/10.1126/science.1159775.

60. McNaughton, B.L., Battaglia, F.P., Jensen, O., Moser, E.I., and Moser, M.-B. (2006). Path integration and the neural basis of the "cognitive map.". Nat. Rev. Neurosci. *7*, 663–678. https://doi.org/10.1038/nrn1932.

61. Campbell, M.G., Attinger, A., Ocko, S.A., Ganguli, S., and Giocomo, L.M. (2021). Distance-tuned neurons drive specialized path integration calculations in medial entorhinal cortex. Cell Rep. *36*, 109669. https://doi.org/10.1016/j.celrep.2021.109669.

62. Kropff, E., Carmichael, J.E., Moser, M.-B., and Moser, E.I. (2015). Speed cells in the medial entorhinal cortex. Nature *523*, 419–424. https://doi.org/10.1038/nature14622.

63. Hinman, J.R., Brandon, M.P., Climer, J.R., Chapman, G.W., and Hasselmo, M.E. (2016). Multiple Running Speed Signals in Medial Entorhinal Cortex. Neuron *91*, 666–679. https://doi.org/10.1016/j.neuron.2016.06.027.

64. Steck, K., Knaden, M., and Hansson, B.S. (2010). Do desert ants smell the scenery in stereo? Anim. Behav. *79*, 939–945. https://doi.org/10.1016/j.anbehav.2010.01.011.

65. Hoy, J.L., Yavorska, I., Wehr, M., and Niell, C.M. (2016). Vision Drives Accurate Approach Behavior during Prey Capture in Laboratory Mice. Curr. Biol. *26*, 3046–3052. https://doi.org/10.1016/j.cub.2016.09.009.

66. Marin, A.C., Schaefer, A.T., and Ackels, T. (2021). Spatial information from the odour environment in mammalian olfaction. Cell Tissue Res. *383*, 473–483. https://doi.org/10.1007/s00441-020-03395-3.

67. McKissick, O., Klimpert, N., Ritt, J.T., and Fleischmann, A. (2024). Odors in space. Front. Neural Circuits *18*, 1414452. https://doi.org/10.3389/fncir.2024.1414452.

68. Barwich, A.-S. (2025). Olfaction is a Spatial Sense. Rev. Philos. Psychol. *16*, 997–1025. https://doi.org/10.1007/s13164-024-00764-7.

69. Ackels, T. (2022). Information about space from time: how mammals navigate the odour landscape. Neuroforum *28*, 159–168. https://doi.org/10.1515/nf-2022-0006.

70. Sterrett, S.C., Findley, T.M., Rafilson, S.E., Brown, M.A., Weible, A.P., Marsden, R., Tarvin, T., Wehr, M., Murray, J.M., Fairhall, A.L., et al. (2025). Olfactory bulb tracks breathing rhythms and place in freely behaving mice. eLife *14*. https://doi.org/10.7554/eLife.105088.1.

71. Poo, C., Agarwal, G., Bonacchi, N., and Mainen, Z.F. (2022). Spatial maps in piriform cortex during olfactory navigation. Nature *601*, 595–599. https://doi.org/10.1038/s41586-021-04242-3.

72. Gretenkord, S., Kostka, J.K., Hartung, H., Watznauer, K., Fleck, D., Minier-Toribio, A., Spehr, M., and Hanganu-Opatz, I.L. (2019). Coordinated electrical activity in the olfactory bulb gates the oscillatory entrainment of entorhinal networks in neonatal mice. PLoS Biol. *17*, e2006994. https://doi.org/10.1371/journal.pbio.2006994.

73. Sosulski, D.L., Bloom, M.L., Cutforth, T., Axel, R., and Datta, S.R. (2011). Distinct representations of olfactory information in different cortical centres. Nature *472*, 213–216. https://doi.org/10.1038/nature09868.

74. Leitner, F.C., Melzer, S., Lütcke, H., Pinna, R., Seeburg, P.H., Helmchen, F., and Monyer, H. (2016). Spatially segregated feedforward and feedback neurons support differential odor processing in the lateral entorhinal cortex. Nat. Neurosci. *19*, 935–944. https://doi.org/10.1038/nn.4303.

75. Bitzenhofer, S.H., Westeinde, E.A., Zhang, H.B., and Isaacson, J.S. (2022). Rapid odor processing by layer 2 subcircuits in lateral entorhinal cortex. eLife *11*, e75065. https://doi.org/10.7554/eLife.75065.

76. Salimi, M., Tabasi, F., Nazari, M., Ghazvineh, S., Salimi, A., Jamaati, H., and Raoufy, M.R. (2021). The olfactory bulb modulates entorhinal cortex oscillations during spatial working memory. J. Physiol. Sci. *71*, 21. https://doi.org/10.1186/s12576-021-00805-1.

77. Salimi, M., Tabasi, F., Abdolsamadi, M., Dehghan, S., Dehdar, K., Nazari, M., Javan, M., Mirnajafi-Zadeh, J., and Raoufy, M.R. (2022). Disrupted connectivity in the olfactory bulb-entorhinal cortex-dorsal hippocampus circuit is associated with recognition memory deficit in Alzheimer's disease model. Sci. Rep. *12*, 4394. https://doi.org/10.1038/s41598-022-08528-y.

78. Chen, Y.-N., Kostka, J.K., Bitzenhofer, S.H., and Hanganu-Opatz, I.L. (2023). Olfactory bulb activity shapes the development of entorhinal-hippocampal coupling and associated cognitive abilities. Curr. Biol. *33*, 4353–4366.e5. https://doi.org/10.1016/j.cub.2023.08.072.

79. Aronov, D., and Tank, D.W. (2014). Engagement of neural circuits underlying 2D spatial navigation in a rodent virtual reality system. Neuron *84*, 442–456. https://doi.org/10.1016/j.neuron.2014.08.042.

80. Low, R.J., Gu, Y., and Tank, D.W. (2014). Cellular resolution optical access to brain regions in fissures: imaging medial prefrontal cortex and grid cells in entorhinal cortex. Proc. Natl. Acad. Sci. USA *111*, 18739–18744. https://doi.org/10.1073/pnas.1421753111.

81. Dubanet, O., and Higley, M.J. (2024). Retrosplenial inputs drive visual representations in the medial entorhinal cortex. Cell Rep. *43*, 114470. https://doi.org/10.1016/j.celrep.2024.114470.

82. Butler, W.N., Hardcastle, K., and Giocomo, L.M. (2019). Remembered reward locations restructure entorhinal spatial maps. Science *363*, 1447–1452. https://doi.org/10.1126/science.aav5297.

83. Boccara, C.N., Nardin, M., Stella, F., O'Neill, J., and Csicsvari, J. (2019). The entorhinal cognitive map is attracted to goals. Science *363*, 1443–1447. https://doi.org/10.1126/science.aav4837.

84. Grienberger, C., and Magee, J.C. (2022). Entorhinal cortex directs learning-related changes in CA1 representations. Nature *611*, 554–562. https://doi.org/10.1038/s41586-022-05378-6.

85. Heys, J.G., and Dombeck, D.A. (2018). Evidence for a subcircuit in medial entorhinal cortex representing elapsed time during immobility. Nat. Neurosci. *21*, 1574–1582. https://doi.org/10.1038/s41593-018-0252-8.

86. Heys, J.G., Wu, Z., Allegra Mascaro, A.L., and Dombeck, D.A. (2020). Inactivation of the Medial Entorhinal Cortex Selectively Disrupts Learning of Interval Timing. Cell Rep. *32*, 108163. https://doi.org/10.1016/j.celrep.2020.108163.

87. Aronov, D., Nevers, R., and Tank, D.W. (2017). Mapping of a non-spatial dimension by the hippocampal-entorhinal circuit. Nature *543*, 719–722. https://doi.org/10.1038/nature21692.

88. Nguyen, D., Wang, G., Wafa, T., Fitzgerald, T., and Gu, Y. (2024). The medial entorhinal cortex encodes multisensory spatial information. Cell Rep. *43*, 114813. https://doi.org/10.1016/j.celrep.2024.114813.

89. Tian, J., Wen, S., Zhou, Y., Hu, N., Yao, S., Zhang, X., Liu, Y., He, Y., Wang, Z., and Miao, C. (2024). Differential Impact of Multiple Sensory Deprivation on Spatial-coding Cells in Medial Entorhinal Cortex. Preprint at bioRxiv. https://doi.org/10.1101/2024.09.09.611946.

90. Butola, T., Hernández-Frausto, M., Blankvoort, S., Flatset, M.S., Peng, L., Hairston, A., Johnson, C.D., Elmaleh, M., Amilcar, A., Hussain, F., et al. (2025). Hippocampus shapes entorhinal cortical output through a direct feedback circuit. Nat. Neurosci. *28*, 811–822. https://doi.org/10.1038/s41593-025-01883-9.

91. Bonnevie, T., Dunn, B., Fyhn, M., Hafting, T., Derdikman, D., Kubie, J.L., Roudi, Y., Moser, E.I., and Moser, M.-B. (2013). Grid cells require excitatory drive from the hippocampus. Nat. Neurosci. *16*, 309–317. https://doi.org/10.1038/nn.3311.

92. van Strien, N.M., Cappaert, N.L.M., and Witter, M.P. (2009). The anatomy of memory: an interactive overview of the parahippocampal-hippocampal network. Nat. Rev. Neurosci. *10*, 272–282. https://doi.org/10.1038/nrn2614.

93. Biella, G., and de Curtis, M. (2000). Olfactory inputs activate the medial entorhinal cortex via the hippocampus. J. Neurophysiol. *83*, 1924–1931. https://doi.org/10.1152/jn.2000.83.4.1924.

94. Young, B.J., Otto, T., Fox, G.D., and Eichenbaum, H. (1997). Memory representation within the parahippocampal region. J. Neurosci. *17*, 5183–5195. https://doi.org/10.1523/JNEUROSCI.17-13-05183.1997.

95. Kitanishi, T., and Matsuo, N. (2017). Organization of the Claustrum-to-Entorhinal Cortical Connection in Mice. J. Neurosci. *37*, 269–280. https://doi.org/10.1523/JNEUROSCI.1360-16.2016.

96. Connor, C.E., and Knierim, J.J. (2017). Integration of objects and space in perception and memory. Nat. Neurosci. *20*, 1493–1503. https://doi.org/10.1038/nn.4657.

97. LaChance, P.A., Todd, T.P., and Taube, J.S. (2019). A sense of space in postrhinal cortex. Science *365*, eaax4192. https://doi.org/10.1126/science.aax4192.

98. Quiroga, R.Q., Reddy, L., Kreiman, G., Koch, C., and Fried, I. (2005). Invariant visual representation by single neurons in the human brain. Nature *435*, 1102–1107. https://doi.org/10.1038/nature03687.

99. Quiroga, R.Q. (2012). Concept cells: the building blocks of declarative memory functions. Nat. Rev. Neurosci. *13*, 587–597. https://doi.org/10.1038/nrn3251.

100. Quian Quiroga, R. (2023). An integrative view of human hippocampal function: Differences with other species and capacity considerations. Hippocampus *33*, 616–634. https://doi.org/10.1002/hipo.23527.

101. Bernardi, S., Benna, M.K., Rigotti, M., Munuera, J., Fusi, S., and Salzman, C.D. (2020). The Geometry of Abstraction in the Hippocampus and Prefrontal Cortex. Cell *183*, 954–967.e21. https://doi.org/10.1016/j.cell.2020.09.031.

102. Nieh, E.H., Schottdorf, M., Freeman, N.W., Low, R.J., Lewallen, S., Koay, S.A., Pinto, L., Gauthier, J.L., Brody, C.D., and Tank, D.W. (2021). Geometry of abstract learned knowledge in the hippocampus. Nature *595*, 80–84. https://doi.org/10.1038/s41586-021-03652-7.

103. Samborska, V., Butler, J.L., Walton, M.E., Behrens, T.E.J., and Akam, T. (2022). Complementary task representations in hippocampus and prefrontal cortex for generalizing the structure of problems. Nat. Neurosci. *25*, 1314–1326. https://doi.org/10.1038/s41593-022-01149-8.

104. Burwell, R.D. (2000). The parahippocampal region: corticocortical connectivity. Ann. N. Y. Acad. Sci. *911*, 25–42. https://doi.org/10.1111/j.1749-6632.2000.tb06717.x.

105. Knierim, J.J., Lee, I., and Hargreaves, E.L. (2006). Hippocampal place cells: parallel input streams, subregional processing, and implications for episodic memory. Hippocampus *16*, 755–764. https://doi.org/10.1002/hipo.20203.

106. Eichenbaum, H., Yonelinas, A.P., and Ranganath, C. (2007). The medial temporal lobe and recognition memory. Annu. Rev. Neurosci. *30*, 123–152. https://doi.org/10.1146/annurev.neuro.30.051606.094328.

107. Kerr, K.M., Agster, K.L., Furtak, S.C., and Burwell, R.D. (2007). Functional neuroanatomy of the parahippocampal region: the lateral and medial entorhinal areas. Hippocampus *17*, 697–708. https://doi.org/10.1002/hipo.20315.

108. Sosa, M., Plitt, M.H., and Giocomo, L.M. (2025). A flexible hippocampal population code for experience relative to reward. Nat. Neurosci. *28*, 1497–1509. https://doi.org/10.1038/s41593-025-01985-4.

109. El-Gaby, M., Harris, A.L., Whittington, J.C.R., Dorrell, W., Bhomick, A., Walton, M.E., Akam, T., and Behrens, T.E.J. (2024). A cellular basis for mapping behavioural structure. Nature *636*, 671–680. https://doi.org/10.1038/s41586-024-08145-x.

110. Rossier, J., Haeberli, C., and Schenk, F. (2000). Auditory cues support place navigation in rats when associated with a visual cue. Behav. Brain Res. *117*, 209–214. https://doi.org/10.1016/s0166-4328(00)00293-x.

111. Watanabe, S., and Yoshida, M. (2007). Auditory cued spatial learning in mice. Physiol. Behav. *92*, 906–910. https://doi.org/10.1016/j.physbeh.2007.06.019.

112. Funamizu, A., Kuhn, B., and Doya, K. (2016). Neural substrate of dynamic Bayesian inference in the cerebral cortex. Nat. Neurosci. *19*, 1682–1689. https://doi.org/10.1038/nn.4390.

113. Gao, S., Webb, J., Mridha, Z., Banta, A., Kemere, C., and McGinley, M. (2020). Novel Virtual Reality System for Auditory Tasks in Head-fixed Mice. Annu. Int. Conf. IEEE Eng. Med. Biol. Soc. *2020*, 2925–2928. https://doi.org/10.1109/EMBC44109.2020.9176536.

114. Sofroniew, N.J., Cohen, J.D., Lee, A.K., and Svoboda, K. (2014). Natural whisker-guided behavior by head-fixed mice in tactile virtual reality. J. Neurosci. *34*, 9537–9550. https://doi.org/10.1523/JNEUROSCI.0712-14.2014.

115. Guyoton, M., Matteucci, G., Foucher, C.G., Getz, M.P., Gjorgjieva, J., and El-Boustani, S. (2025). Cortical circuits for cross-modal generalization. Nat. Commun. *16*, 4230. https://doi.org/10.1038/s41467-025-59342-9.

116. Vickers, N.J., Christensen, T.A., Baker, T.C., and Hildebrand, J.G. (2001). Odour-plume dynamics influence the brain's olfactory code. Nature *410*, 466–470. https://doi.org/10.1038/35068559.

117. Chen, T.-W., Wardill, T.J., Sun, Y., Pulver, S.R., Renninger, S.L., Baohan, A., Schreiter, E.R., Kerr, R.A., Orger, M.B., Jayaraman, V., et al. (2013). Ultrasensitive fluorescent proteins for imaging neuronal activity. Nature *499*, 295–300. https://doi.org/10.1038/nature12354.

118. Wekselblatt, J.B., Flister, E.D., Piscopo, D.M., and Niell, C.M. (2016). Large-scale imaging of cortical dynamics during sensory perception and behavior. J. Neurophysiol. *115*, 2852–2866. https://doi.org/10.1152/jn.01056.2015.

119. Kaufman, A.M., Geiller, T., and Losonczy, A. (2020). A Role for the Locus Coeruleus in Hippocampal CA1 Place Cell Reorganization during Spatial Reward Learning. Neuron *105*, 1018–1026.e4. https://doi.org/10.1016/j.neuron.2019.12.029.

120. Pachitariu, M., Stringer, C., Dipoppa, M., Schröder, S., Rossi, L.F., Dalgleish, H., Carandini, M., and Harris, K.D. (2017). Suite2p: beyond 10,000 neurons with standard two-photon microscopy. Preprint at bioRxiv. https://doi.org/10.1101/061507.

121. Dombeck, D.A., Khabbaz, A.N., Collman, F., Adelman, T.L., and Tank, D.W. (2007). Imaging large-scale neural activity with cellular resolution in awake, mobile mice. Neuron *56*, 43–57. https://doi.org/10.1016/j.neuron.2007.08.003.

122. Climer, J.R., and Dombeck, D.A. (2021). Information theoretic approaches to deciphering the neural code with functional fluorescence imaging. eNeuro *8*. ENEURO.0266-21.2021. https://doi.org/10.1523/ENEURO.0266-21.2021.

123. Gothard, K.M., Skaggs, W.E., Moore, K.M., and McNaughton, B.L. (1996). Binding of hippocampal CA1 neural activity to multiple reference frames in a landmark-based navigation task. J. Neurosci. *16*, 823–835. https://doi.org/10.1523/JNEUROSCI.16-02-00823.1996.

124. Zhang, K., Ginzburg, I., McNaughton, B.L., and Sejnowski, T.J. (1998). Interpreting neuronal population activity by reconstruction: unified framework with application to hippocampal place cells. J. Neurophysiol. *79*, 1017–1044. https://doi.org/10.1152/jn.1998.79.2.1017.

125. Etter, G., Manseau, F., and Williams, S. (2020). A Probabilistic Framework for Decoding Behavior From in vivo Calcium Imaging Data. Front. Neural Circuits *14*, 19. https://doi.org/10.3389/fncir.2020.00019.

126. Brown, E.N., Barbieri, R., Eden, U.T., and Frank, L.M. (2003). Likelihood methods for neural spike train data analysis. In Computational Neuroscience: A Comprehensive Approach, J. Feng, ed. (CRC Press), pp. 252–281. https://doi.org/10.1201/9780203494462.ch9.

127. Friedrich, J., Zhou, P., and Paninski, L. (2017). Fast online deconvolution of calcium imaging data. PLOS Comput. Biol. *13*, e1005423. https://doi.org/10.1371/journal.pcbi.1005423.

128. Azzalini, A. (2005). The Skew-normal Distribution and Related Multivariate Families. Scand. J. Stat. *32*, 159–188. https://doi.org/10.1111/j.1467-9469.2005.00426.x.

129. Yates, L.A., Richards, S.A., and Brook, B.W. (2021). Parsimonious model selection using information theory: a modified selection rule. Ecology *102*, e03475. https://doi.org/10.1002/ecy.3475.

STAR★METHODS

KEY RESOURCES TABLE

REAGENT or RESOURCE	SOURCE	IDENTIFIER
Bacterial and virus strains		
pAAV.Syn.GCaMP6f.WPRE.SV40 (AAV1)	Reference[117]	Addgene:100837-AAV1 (RRID:Addgene_100837)
Experimental models: Organisms/strains		
tetO-GCaMP6s mice	Jackson Lab.	JAX-024742 (RRID:IMSR_JAX:024742)
Camk2a-tTA mice	Jackson Lab.	JAX-007004 (RRID:IMSR_JAX:007004)
Software and algorithms		
MATLAB	MathWorks	https://www.mathworks.com
ScanImage 5.1	MBF Bioscience	https://www.mbfbioscience.com/products/scanimage
Clampex 10.3	Molecular Devices	https://www.moleculardevices.com/
Suite2P	Harris Lab	https://github.com/MouseLand/suite2p
ViRMEn	Tank Lab	https://github.com/Tank-Lab/ViRMEn
FINDBN	Dombeck Lab	https://github.com/DombeckLab/Issa2023
MLE Conjunctive	Dombeck Lab	https://github.com/DombeckLab/mle_conjunctive
Deposited data		
Custom code and preprocessed imaging data	Zenodo	https://zenodo.org/records/18734619

EXPERIMENTAL MODEL AND STUDY PARTICIPANT DETAILS

Mice

All experimental procedures were approved by the Northwestern University Institutional Animal Care and Use Committee. To image neural populations in the LEC and MEC, we bred and used transgenic mice expressing GCaMP6s, generated by crossing tetO-GCaMP6s mice[118] (JAX catalog no. 024742) with Camk2a-tTA mice (JAX catalog no. 007004). For CA1 imaging, these mice received adeno-associated virus (AAV) injections as described below. The number of female/male animals used per region was as follows: CA1 (3M), LEC (2M/4F), and MEC (5M/1F). No differences in findings were noted between male and female mice.

METHOD DETAILS

Multisensory Virtual Reality (VR) apparatus

We employed our previously described custom multisensory VR system,[17,50] which enables precise and independent manipulation of visual and olfactory cues. Head-fixed mice ran on a cylindrical treadmill positioned in front of a five-panel monitor array. Treadmill velocity was measured using a rotary encoder (US Digital E2-5000) and sampled in MATLAB at a VR engine refresh rate of approximately 5 ms via a National Instruments PCI-6229 data acquisition card. The treadmill rotation signal was scaled to correspond to virtual distance (63.8 cm per revolution). Visual environments were generated in MATLAB using ViRMEn[79] with cylindrical transformation. The environment consisted of parallel transparent walls featuring white spot patterns to generate optic flow and a single large green arch serving as a spatial visual landmark. The virtual track extended infinitely, with the visual target defined as the crossing of the front plane of the visual landmark.

Olfactory stimuli were delivered using mass flow controllers (MFCs; Alicat MC-100SCCM-D for odorant, flow range 0–0.1 L/min; MC-15SLPM-D for carrier air, flow range 0–1 L/min). The odorant solution (12 mL α-pinene diluted in mineral oil at 1:37.5, Sigma-Aldrich) was housed in a sealed 40 mL vial filled with glass beads and mixed with carrier air in a passive mixing chamber. The resulting odor-air mixture was delivered into a 0.07 cm^3 nose chamber positioned around the mouse's snout. Odor concentration was dynamically modulated (1%–100%) via the odorant MFC, with the carrier stream adjusted in tandem to maintain a constant total flow rate of 1.000 L/min. Along the virtual track, the odor concentration followed a linear spatial gradient with peak centered at the odor landmark (x_o):

$$[odorant] = 100\% - \frac{99\%}{6\,m}|x - x_o|$$

here, x denotes the mouse's position, and x_0 marks the location of the odor landmark. Both the gradient slope and the peak concentration were held constant, enabling the mouse to estimate the landmark's location from any position along the track. To improve spatial accuracy, a predictive algorithm estimated the mouse's future position 183 ms ahead, compensating for olfactometer delay, and adjusted odor delivery accordingly at each VR iteration.

Licks were detected using a capacitive sensing circuit (SparkFun) connected to a water spout placed within the reach of the mouse's tongue, and were recorded in MATLAB via a National Instruments PCI-6229 card. All task components, including visual stimuli, MFC control, and reward delivery, were controlled through the ViRMEn engine in MATLAB software. A Digidata 1440A system (Molecular Devices; Clampex 10.3) recorded and synchronized all signals at 1 kHz, including virtual track position, MFC flow rates, licking events, reward delivery, visual and odor landmark encounters, and two-photon imaging frame times.

CA1 surgery

Mice were anesthetized with isoflurane (3% for induction, 1%–2% for maintenance in 0.5 L/min O_2), with body temperature maintained at 37 °C and ophthalmic ointment applied to prevent corneal drying. To reduce inflammation and manage pain, dexamethasone (5 mg/kg) and buprenorphine-SR-LAB (1 mg/kg subcutaneous) were administered, along with saline (0.5–1.0 mL) to prevent dehydration. A small craniotomy (~0.5 mm diameter) was made at coordinates 2.3 mm caudal and 1.8 mm lateral (right hemisphere) relative to Bregma. To express GCaMP6f[117] in CA1 pyramidal neurons, we injected pAAV.Syn.GCaMP6f.WPRE.SV40 (Addgene #100837-AAV1; diluted ~10× from a 2×10^{13} GC/mL stock in PBS) to a depth of 1.3 mm below the dura using a beveled glass micropipette. Typically, 60 nL of viral solution was injected at the level of the CA1 stratum pyramidale. Two to four days later, a second surgery was performed to implant a stainless-steel cannula with an attached 2.5 mm No. 1 glass coverslip (affixed with NOA81 adhesive, Norland; Potomac Photonics) above the hippocampus.[56] A titanium headplate was secured to the skull using dental cement (Metabond, Parkell). Mice were monitored postoperatively for 24 h and allowed to recover for 3–5 days before beginning water scheduling (0.9–1.0 mL/day) and behavioral training.

LEC surgery

Prism implantation for LEC imaging was performed according to our previously described protocol.[24] As the LEC is a lateral region, we used a microprism to rotate the imaging plane by 90°, enabling optical access from above. A 3 mm craniotomy centered 3.5 mm caudal to Bregma was performed over the right lateral skull, positioned as far ventral as possible to cross beyond the rhinal fissure. A 3 mm round No. 0 coverslip (CS-3R-0, Warner Instruments) was temporarily held in place using a micromanipulator-mounted pipette (1.0 mm diameter, Q100-70-7.5, Sutter Instrument) and secured with dental cement (Metabond, Parkell). UV-curable adhesive (NOA81, Norland; UV source: CS20K2, Thorlabs) was then used to affix a 2.0 mm microprism (MPCH-2.0, Tower Optical) to the external surface of the coverslip. Additional dental cement was applied to seal any remaining gaps and to attach a titanium headplate.

MEC surgery

Prism implantation for MEC imaging followed our established protocol.[24,57] A 2–3 mm craniotomy was performed over the right cerebellum. Next, a 2 mm incision was made in the cerebellar dura along the posterior edge of the transverse sinus, and a small amount of cerebellum was aspirated to expose the caudal cortical surface. A 45° microprism (1.5 mm or 2.0 mm; MPCH-1.5 or MPCH-2.0, Tower Optical) mounted onto a custom stainless-steel holder using UV-curable adhesive (NOA81, Norland) was positioned such that its front face contacted the MEC. The prism assembly was then secured with dental cement while applying gentle anterior pressure to enhance stability of the window. A titanium headplate was then attached with dental cement.

Behavior

Water-scheduled mice received 0.9–1.0 mL of water per day, with daily monitoring of body weight and overall health. Starting approximately three days after cannula implantation, mice underwent daily training sessions (30–45 minutes) on the multisensory VR system, performing one of three navigation tasks: olfactory-guided, visually guided, or first-target guided.[17] In each task, head-fixed mice navigated a one-dimensional multisensory virtual environment by running on a treadmill and received water rewards upon reaching a task-specific target, i.e., the odor landmark, the visual landmark, or the first of the two. Mice typically acquired the olfactory-guided and visually guided tasks within 1–2 weeks, as evidenced by consistent anticipatory licking and slowing behaviors before reaching the target. For the first-target guided task, mice were first trained on the olfactory-guided task for over a week before transitioning to the combined task, reaching criterion performance within an additional 6–9 sessions. Some mice where imaged in multiple tasks.

In each trial, the visual landmark was randomly placed at one of seven possible locations along the track: 2.40, 3.00, 3.60, 4.20, 4.80, 5.40, or 6.00 m from the start. The odor target was positioned randomly at a distance of 1.15–2.99 m either before or after the visual landmark. If the selected position placed the odor target too close to the start (<2 m) or beyond the end of the track (>6 m), it was re-sampled. Total track lengths varied from 3.55 to 6.00 m (mean ± SEM: 5.26 ± 0.64 m), with inter-landmark distances ranging from 1.15 to 2.99 m (2.01 ± 0.48 m). Water rewards (2 μL each) were delivered via a solenoid valve calibrated by its open duration (typically 20 ms). The valve was housed in sound-dampening foam outside the behavioral chamber, and white noise was played during sessions to mask any auditory cues associated with reward delivery. Each trial concluded when the mouse reached the second landmark. At the end of the trial, both visual and olfactory stimuli were frozen for 1 second, followed by a 2-second "washout" period

during which the screen turned black and odor concentration was reduced to the minimum (1%). After washout, the mouse was automatically returned to the starting position for the next trial.

Two-photon imaging

Imaging sessions began once mice reached stable task performance. Criteria for imaging included: (1) a behavioral rate exceeding two laps per minute on average during 30–50-minute sessions, and (2) consistent anticipatory behaviors across sessions, such as pre-reward licking and slowing. To ensure high-quality behavioral data, imaging in a particular session commenced only after the animal completed several correct trials displaying robust pre-reward licking. All sessions were monitored in real time by the experimenter, and all mice exhibited sufficient anticipatory behavior to be included in further analyses.

Two-photon calcium imaging was conducted using a custom-built, moveable-objective two-photon microscope equipped with a resonant scanner (Sutter Instruments) and a 20X objective (LUCPlanFL N, Olympus). Excitation was provided by a mode-locked Ti:Sapphire laser tuned to 920 nm (Chameleon Ultra II, Coherent), delivering approximately 100-150 mW of average power out of the objective. Emitted fluorescence was separated using a 560 nm longpass dichroic mirror (FF560-Di01, Semrock) into green (FF01-510/84, Semrock) and red (FF01-620/52, Semrock) channels and detected by GaAsP photomultiplier tubes (H10770PA-40, Hamamatsu Photonics). Image acquisition was controlled via ScanImage (Vidrio Technologies). Time-series recordings typically consisted of 16,000 frames at 512 $\times$ 256 pixels (0.0675 ms/line), acquired at 58.4 Hz. Most sessions ranged from 64,000 to 96,000 total frames. For LEC and MEC prism imaging, the field of view ranged from 300 $\times$ 300 μm to 600 $\times$ 600 μm, with imaging typically performed at 1.1X to 1.9X magnification.

To minimize contamination from the VR monitor's light, a custom light-shielding cylinder made from opaque electrical tape was positioned between the headbar and the microscope objective.

QUANTIFICATION AND STATISTICAL ANALYSIS

Statistics and reproducibility

All data analyses were performed using custom-written software in MATLAB (MathWorks). Although statistical methods were not used to predetermine sample sizes, the number of subjects was consistent with prior publications.[17,24,119] The experimenter was not blinded to experimental conditions during data collection or analysis due to the necessity of anatomical targeting for imaging, which made blinding impractical. Inclusion criteria were based on predefined behavioral performance metrics, and all mice with high-quality imaging windows and satisfactory task performance were included in the analysis.

Only non-parametric statistical tests were used, with no assumptions about underlying data distributions. These included bootstrapping, Wilcoxon signed-rank tests, Wilcoxon rank-sum tests, and chi-square goodness-of-fit tests, applied where appropriate. For multiple comparisons using the Wilcoxon rank-sum test, uncorrected p-values are reported, with Bonferroni-corrected thresholds for statistical significance indicated in figure legends. Statistical significance was defined as $p < 0.05$, except for neuron-type classification analyses, where a stricter criterion of $p < 0.01$ was applied. While data distributions were assumed to be approximately normal, no formal tests for normality were conducted. All quantitative results are reported in the main text and figure legends, including definitions of sample size (n), measures of central tendency, and statistical significance thresholds. Unless otherwise specified, values are reported as mean ± SEM. Cross-validation was performed by comparing results from odd and even trials, and analyses were conducted both at the session level and across animals to assess generalizability. Imaging experiments across brain regions were conducted using identical experimental protocols and analysis pipelines. Regional comparisons were not randomized, as recordings for each area were typically carried out in dedicated experimental batches.

Behavioral analysis

At each time point, the mouse occupied a single position, defined as its distance from the start of the virtual track. To align behavioral and neural data with task-relevant landmarks, we calculated relative position vectors by subtracting the location of each landmark, i.e., start, visual landmark, odor landmark, first landmark, or second landmark, from the current position. Our primary behavioral metric was pre-target licking, used to quantify anticipatory behavior. To isolate anticipatory licks from consummatory licks, we excluded all licks that occurred after reward delivery, within 0.25 m beyond the reward site, or within 0.25 m of the start position. Behavioral sessions were included only if they met two criteria:

Target-selective licking

increased lick rates prior to the rewarded target compared to the non-rewarded landmark. For each session, we divided the track into 25-cm bins centered on each landmark and computed lick rates as the number of licks divided by the time spent in each bin. Pre-target licking was defined as the lick rate in the 25-cm bin immediately before the rewarded landmark. Sessions were included if mice exhibited significantly greater pre-target licking for the rewarded versus non-rewarded target across trials, assessed using Wilcoxon signed-rank tests.

Navigation strategy

To distinguish sensory-guided navigation from path integration, we assessed whether mice adjusted the location of their licking based on the landmark position. For each trial, we computed the median lick position occurring between the start and the rewarded target. We then plotted this median position in both start-aligned and target-aligned coordinates against the distance between start

and target. Spearman correlation coefficients were calculated: R-start (correlation in start-aligned coordinates) and R-target (correlation in target-aligned coordinates). Sessions were classified as sensory-guided if R-start > R-target, indicating lick position was dependent on the location of the target rather than a fixed distance from the start. For the first-target guided task, this analysis was performed separately for visual-first and odor-first trials to confirm strategy consistency across modalities.

Only sessions that met both criteria, i.e., pre-target licking and non-path-integrative navigation, were included in the final dataset.

Calcium Imaging analysis

We applied the following analysis pipeline using custom MATLAB code. First, motion correction, ROI segmentation, and raw fluorescence extraction were performed using a Python implementation of Suite2p.[120,121] For each ROI, we extracted the raw fluorescence vs time trace along with a corresponding neuropil signal. A small fraction of traces were removed due to out of range min, max, and mean values. We then applied an integrated, iterative algorithm[24] to calculate $\Delta F/F_o$ by estimating the neuropil contamination ratio and baseline fluorescence (F_o). Next, significant calcium transients were calculated from $\Delta F/F_o$[121] and this signal was used for the subsequent calculations throughout the papers.

Behavioral data were downsampled to match the imaging frame rate (58.4 Hz) and aligned with the timing of significant calcium transients. To isolate activity related to active navigation, we restricted the analysis to time points when the animal was making forward progress along the track (> 10 cm/s). Only movement-associated calcium events were included in subsequent neural analyses, excluding periods of rest, reward consumption, or inter-trial intervals.

Spatial information calculation and spatial cell type classification

To identify active neurons, we first computed the average $\Delta F/F_o$ signal for each cell across all laps and time points within a session. Neurons were classified as "active" if they contained significant calcium transients on at least 1/3 of laps. Imaging sessions that contained more than 50 active cells were considered for further analysis. Spatial information of each individual cell was calculated using our previously established method.[17,122] Only imaging frames corresponding to running periods (> 10 cm/s) were included in the analysis. Spatial information content was computed for each neuron using the following formula:

$$SI = \frac{1}{f}\sum_{i=1}^{N} f_i p_x(x_i)\log_2\left(\frac{f_i}{f}\right)$$

where SI is the spatial information in bits per event, N is the total number of spatial bins (60 bins, bin width = 25 cm), f_i is the mean fluorescence (inferred firing) in bin i, f is the overall mean fluorescence across all bins, and $p_x(x_i)$ is the occupancy probability of bin i. This calculation was performed independently for each spatial reference frame: position relative to the start, the visual landmark, the odor landmark, and the first landmark. As a control, spatial information was also calculated relative to the second landmark in first-target guided navigation sessions.

To classify neurons as start-, odor-, visual-, or first-target–spatial, we adapted a method based on previous approaches.[17,123] For each neuron, we identified the spatial reference frame (e.g., start, visual, olfactory, or first target) in which the neuron exhibited the highest spatial information score. To determine whether this tuning exceeded chance, we generated a null distribution by shuffling the neuron's significant transient trace. The trace was divided into $\geq$ 100 segments (preserving the shape and timing of individual transients), randomly reordered, and then recombined. Spatial information was then recalculated using the original position vector. This process was repeated 1,000 times. The p-value was defined as the proportion of shuffled information values that exceeded the actual observed score. Neurons with $p < 0.01$ in their highest-scoring spatial frame were classified as spatially tuned to that coordinate. Neurons that met this criterion were classified as "spatial cells", with no minimum spatial information threshold used. In contrast, neurons that did not meet this threshold were labeled "none." Although some neurons exhibited significant spatial information in multiple frames, we did not classify them as conjunctive (e.g., olfactory-visual) because the spatial reference frames were not fully independent. For example, strong tuning to the visual landmark could artificially elevate spatial information in the odor coordinate due to the fixed inter-landmark distance (1.15–2.99 m), rather than reflecting true multimodal selectivity. For a better visualization of population heatmaps, the spatial tuning of individual spatial cells were smoothed using a sliding window of 3 bins (each bin width = 25 cm).

Bayesian reconstruction

To assess the accuracy of spatial representations across CA1, LEC, and MEC, we used Bayesian decoding methods.[17,124,125] The virtual track was divided into 10 cm bins, and data were split into training (odd-numbered trials) and testing (even-numbered trials) sets. For single-trial decoding, we applied leave-one-out cross-validation, training the decoder on all but one trial and evaluating performance on the held-out trial. Each session was divided into time bins of $\Delta t = 0.1$ s. For each time bin n, we estimated the conditional probability that the animal was at position bin x_i (width = 25 cm) given the observed significant transients, using the following formulation:

$$p(x_i|n) = p_X(x_i)\left(\prod_{j=1}^{M} f_{i,j}^{n_j}\right)e^{-\Delta t\sum_{j=1}^{M} f_{i,j}}$$

where $p(x_i|n)$ is the occupancy probability of bin x_i, $f_{i,j}$ is the average transient rate of neuron j in bin x_is n_j is the number of transients from neuron j in time bin n, M is the total number of neurons. The decoded position was taken as the bin with the highest posterior probability. Decoding was performed separately using four coordinate systems: distance from the start, from the visual landmark, from the odor landmark, and from the first landmark. As a control, decoding was also performed using distance from the second landmark in the first-target guided navigation task. To establish a chance-level baseline, decoded positions were randomly shuffled across time bins within each trial. Reconstruction error was computed as the Euclidean distance between the real (non-binned) and decoded positions at each time point. The median decoding error within each spatial bin along the track was used due to its robustness against outliers, particularly at the track edges where decoding variability tends to increase. This procedure was repeated for both the original and shuffled data. To compare decoding accuracy across navigation conditions, we used Wilcoxon rank-sum tests applied separately within each spatial bin. A decoding condition was considered significantly more accurate in a given bin if its median error was lower than that of all other conditions ($p < 0.05$).

Maximum likelihood estimation (MLE) for conjunctivity analysis

To identify conjunctive spatial tuning beyond what could arise from overlapping coordinate systems (e.g., start, visual, odor, and first-target coordinates), we employed an MLE framework,[17,126] modeling each neuron's spiking activity as an inhomogeneous Poisson process. First, calcium traces ($\Delta F/F_0$) from each neuron, including both significant and non-significant transients, were deconvolved using a first-order autoregressive model (AR(1)) with a hard threshold (ℓ_0 penalty) to estimate continuous activity.[127] Noise levels and the decay constant were initialized manually ($\tau = 0.58$ s). These deconvolved traces were converted into pseudo-spike counts by identifying events that coincided with both a significant transient and a deconvolution peak. A unit pseudo-spike was defined as the median amplitude of the lowest 5% of such events; if insufficient events were present, the smallest was used. All deconvolved values were linearly scaled to this unit and rounded to the nearest integer to yield frame-wise pseudo-spike counts. While this transformation does not claim to capture true spike rates precisely, it provides a reliable and unbiased estimate of relative spiking, allowing consistent comparisons across spatial reference frames within each neuron.

Each neuron's pseudo-spike rate was modeled as the sum of a skewed multivariate Gaussian tuning function for each field[128]:

$$f(x;\ \xi, \alpha, \Omega)\ =\ 2\phi_d(x\ -\ \xi; \Omega)\Phi\left(\alpha^T\omega^{-1}\ (x\ -\ \xi)\right), y\ \in\ \mathbb{R}^d$$

where ξ is a d dimensional location parameter, α is a d dimensional shape parameter, Ω is a positive definite matrix, ϕ_d is the density function of a $N_d(0, \Omega)$ variable, and Φ is the cumulative distribution function of a $N(0, 1)$ variable.

The covariance matrix of the distribution is $\Omega\ -\ \omega\mu_z\mu_z^T\omega$ and the skewness is $\gamma\ =\ \left(\frac{4-\pi}{2}\right)^2\left(\frac{\mu_z^T\overline{\Omega}\mu_z}{1-\mu_z^T\overline{\Omega}\mu_z}\right)^3$, where $\mu_z\ =\ \sqrt{\frac{2}{\pi}}\left(1+a^T\overline{\Omega}a\right)^{-\frac{1}{2}}\overline{\Omega}a$ and $\overline{\Omega}$ is the correlation matrix associated with Ω. Twice the square root of the eigenvalues of the covariance matrix were used as the widths of the field along its major and minor axes and the eigenvectors were used to determine the field orientation.

Each neuron's pseudo-spike rate was modeled with the conditional intensity function:

$$\lambda_i\ =\ b + \sum_{j=1}^{2} C_j f\left(x_i; \xi_j, \alpha_j, \Omega_j\right)\ /\ f\left(z_j; \xi_j, \alpha_j, \Omega_j\right)$$

where i is the time bin, b is the baseline rate, j is the field number, C is the peak rate above baseline for the field, x is the position of the animal, and z_j is the mode of the jth field (determined numerically).

The log-likelihood was determined using a Poisson model:

$$LL\ =\ \sum_{i=1}^{n} y_i\ \ln(\lambda_i\Delta t)\lambda_i\Delta t\ -\ \ln(y_i!)$$

where n is the number of imaging frames, y_i is the observed pseudo-spike count at frame i, and Δt is the frame duration (0.01728 s).

The null model was "flat" ($C_1\ =\ C_2\ =\ 0$). We fit up to two-dimensional conjunctions (start-visual, start-odor, start-first, and odor-visual) with the exception of the visual-first and odor-first conjunctions due to redundancy in the definition of these coordinates. For "pure" models (start, visual, odor and first), d=1, and for "conjunctive" models d=2. For each pure and conjunctive dataset, a single field model ($C_1 > 0, C_2\ =\ 0$) and a two-field model ($C_1 > 0$, $C_2 > 0$) was fit. Altogether, 17 models were fit for each neuron. All parameters were optimized using MATLAB's particleswarm algorithm. The solutions were constrained so that the minor width of the field was between 20 and 200 cm, the peak of the distribution was at most one standard deviations away from occupied locations in the d dimensional conjunctive space, at least $^1/_3$ of the spikes were predicted to fall within each field, and the skewness was at most 0.8, the rate on the line between the field centers fell to at least 10% of the peak.

To select the best-fitting model, each model was fit using five-fold cross validation across trials stratified across which landmark occurred first. The best model was selected using the modified one-standard error rule on the resulting loglikelihood[129] and was used to classify the neurons. The MLE approach resulted in eight distinct cell types (i.e., start, visual, odor, first-target, start-visual, start-

odor, start-first, and visual-odor spatial cells). The full (non-cross validated) dataset was then fit with the best-fitting model for further analysis. Sessions that contained more than thirty MLE-identified spatial cells were considered for prevalence analysis across tasks and brain regions.

"AND" and "OR" conjunctive cell identification

To further characterize conjunctive neurons, we analyzed their tuning geometry across regions and task conditions, revealing distinct classes of Boolean-like spatial coding. Based on MLE fits and deconvolved spiking heatmaps, we categorized fields from conjunctive neurons into three types using the field widths and orientations.

1) "AND" Fields: These fields encoded combinations of spatial coordinates in an interdependent manner, responding only when both spatial dimensions (e.g., visual *and* odor) were simultaneously satisfied. These were all fields that did not qualify as "LAP" or "OR" fields.
2) "OR" Fields: These fields strongly encoded a single coordinate, as indicated by appearing as a stripe across the headmap. The major axis was within 30 degrees of the cardinal axis, the eccentricity ($e = \sqrt{1 - w_1^2/w_2^2}$, where w_1 is the length of the minor axis and w_2 is the length of the major axis) was at least 0.8, and the major field axis was at least 100 cm.
3) "LAP" Fields: These less-selective fields aligned to the animals motion through the conjunctive space and reflected activity across full laps. They had an eccentricity of at least 0.8, a major field width of at least 300 cm, and were oriented within 30 degrees of the 1:1 line.

A cell was determined to be an AND cell if all its fields were AND type and an OR cell if at least one of its fields were an OR type. LAP cells were broadly tuned and thus excluded from further conjunctive analysis. Sessions that contained more than a total of ten AND and OR cells were considered for prevalence analysis across tasks and brain regions.